Monthly Notices
of the
ROYAL ASTRONOMICAL SOCIETY

MNRAS **492,** 2208–2228 (2020)
Advance Access publication 2020 January 3

doi:10.1093/mnras/stz3598

LSQ13ddu: a rapidly evolving stripped-envelope supernova with early circumstellar interaction signatures

Peter Clark,[1★] Kate Maguire,[1,2] Cosimo Inserra,[3] Simon Prentice,[1,2] Stephen J. Smartt,[1] Carlos Contreras,[4] Griffin Hossenizadeh,[5] Eric Y. Hsiao,[6] Erkki Kankare,[7] Mansi Kasliwal,[8] Peter Nugent,[9] Melissa Shahbandeh,[6] Charles Baltay,[10] David Rabinowitz,[10] Iair Arcavi,[11] Chris Ashall,[6] Christopher R. Burns,[12] Emma Callis,[13] Ting-Wan Chen,[14] Tiara Diamond,[15] Morgan Fraser,[13] D. Andrew Howell,[16,17] Emir Karamehmetoglu,[18,19] Rubina Kotak,[7] Joseph Lyman,[20] Nidia Morrell,[4] Mark Phillips,[4] Giuliano Pignata,[21,22] Miika Pursiainen,[23] Jesper Sollerman,[19] Maximilian Stritzinger,[18] Mark Sullivan[23] and David Young[1]

Affiliations are listed at the end of the paper

Accepted 2019 December 20. Received 2019 December 20; in original form 2019 March 29

ABSTRACT

This paper describes the rapidly evolving and unusual supernova LSQ13ddu, discovered by the La Silla-QUEST survey. LSQ13ddu displayed a rapid rise of just 4.8 ± 0.9 d to reach a peak brightness of -19.70 ± 0.02 mag in the *LSQgr* band. Early spectra of LSQ13ddu showed the presence of weak and narrow He I features arising from interaction with circumstellar material (CSM). These interaction signatures weakened quickly, with broad features consistent with those seen in stripped-envelope SNe becoming dominant around two weeks after maximum. The narrow He I velocities are consistent with the wind velocities of luminous blue variables but its spectra lack the typically seen hydrogen features. The fast and bright early light curve is inconsistent with radioactive ^{56}Ni powering but can be explained through a combination of CSM interaction and an underlying ^{56}Ni decay component that dominates the later time behaviour of LSQ13ddu. Based on the strength of the underlying broad features, LSQ13ddu appears deficient in He compared to standard SNe Ib.

Key words: circumstellar matter – supernovae: general – supernovae: individual: LSQ13ddu.

1 INTRODUCTION

In recent years transient surveys such as the Asteroid Terrestrial-impact Last Alert System (ATLAS; Tonry et al. 2018), the La-Silla QUEST survey (LSQ; Baltay et al. 2013), the All-Sky Automated Survey for Supernovae (ASAS-SN; Shappee et al. 2014), the Dark Energy Survey (DES; Pursiainen et al. 2018), and the Zwicky Transient Facility (ZTF; Bellm et al. 2019) have used high-cadence observations (repeat visits every ∼1–3 d) to reveal and study new classes of luminous and rapidly evolving transients (Drout et al. 2014; Arcavi et al. 2016). Numerous other objects showing exotic and unusual behaviour have been observed such as iPTF16asu (Whitesides et al. 2017) and AT 2018cow (Prentice et al. 2018b), with these transients presenting challenges to existing explosion models and progenitor scenarios. Transitional objects whose properties span more than one class of transients have also been observed, such as SN 2016coi that had properties consistent with SNe Ic but with evidence of residual He within its ejecta (Prentice et al. 2018a).

There are also known classes of luminous, and sometimes fast-evolving, transients showing clear signs of interaction with circumstellar material (CSM). Type IIn SNe show features associated with H-rich Type II SNe, along with narrow (‘n’) H emission lines superimposed on their spectra (Schlegel 1990). Similarly, SNe Ibn (Pastorello et al. 2008a) are a rare subclass of helium-rich Type Ib SNe that display narrow He emission features within their spectra. These features are produced through interaction between the SN ejecta and surrounding CSM with SNe Ibn showing wide variation in their spectral evolution. Some develop weak H features at late times (Smith et al. 2012; Pastorello et al. 2015a), thought to be indicative of the SN ejecta interacting with a more distant shell of

---

★ E-mail: pclark02@qub.ac.uk

Published by Oxford University Press on behalf of the Royal Astronomical Society

H-rich CSM, while others evolve to more closely resemble ‘normal’ Type Ib SNe displaying broad He features at late times (Pastorello et al. 2015a,d).

Despite their varied spectral evolution, SNe Ibn display broadly similar photometric behaviour (Hosseinzadeh et al. 2017), with an initial rise to a peak *R*-band absolute magnitude between −18.5 and −20 mag over the course of a few days up to two weeks. This rise is then usually followed by a decline over the course of ∼1–2 months. A small subset of SNe Ibn have been observed to have much slower post-maximum decline rates, with OGLE-2012-SN-006 being notable for entering an extended plateau-like phase (Pastorello et al. 2015b). Additionally, one SN Ibn (OGLE-2014-SN-131) was observed to have an extended rise to peak (Karamehmetoglu et al. 2017), though such events form a small proportion of the overall class.

The most popular explanation for the production of SNe Ibn involves the core collapse of a H/He poor WCO-type Wolf–Rayet (WR) star embedded in a He-rich CSM (Foley et al. 2007; Pastorello et al. 2007). The CSM is expected to have velocities consistent with the wind speed of known WR stars of a few thousand km s^{-1}(Rochowicz & Niedzielski 1999; Crowther 2007). Alternatively, the CSM present in these events could originate from material stripped from companion stars with evidence of a luminous blue variable-type (LBV-type) outburst from the system (either the progenitor or companion) of the prototype event SN 2006jc (Pastorello et al. 2007). It has also been suggested that stars within a transitional phase between LBV and WR may be responsible for producing SNe Ibn. The origin of these SNe as core-collapse events is supported by their occurrence within spiral host galaxies suggesting a link to young stellar populations. PS1-12sk is an exception in that it occurred within a bright, cluster hosted elliptical galaxy (Sanders et al. 2013; Pastorello et al. 2015a; Hosseinzadeh et al. 2019).

We present photometric and spectroscopic observations and analysis of the unusual and fast evolving transient, LSQ13ddu. It was discovered by LSQ (Baltay et al. 2013) on MJD 56622.3 at RA = 03:58:49.09 Dec. = −29:25:11.8 (J2000.0), which is offset by 4 kpc in projection from the centre of the galaxy, 2MASX J03584923−2925086 (Jones et al. 2009), an Sc spiral (Makarov et al. 2014) at a redshift of $z = 0.05845 \pm 0.00015$[1] (Fig. 1). Using measurements of host galaxy emission lines in the spectra of LSQ13ddu at the position of SN, we find a slightly lower redshift of $z = 0.057787 \pm 0.000125$, which we use throughout this paper. LSQ13ddu was observed spectroscopically three days after the discovery by the Public ESO Spectroscopic Survey of Transient Objects (PESSTO; Smartt et al. 2014). Due to its rapid rise in brightness and unusual early-time spectra, an extensive follow-up campaign was triggered. Throughout this paper, we assume a Hubble constant, H_0 of 70 km s^{-1} Mpc^{-1} and adopt a standard cosmology with $\Omega_M = 0.27$ and $\Omega_\Lambda = 0.73$.

2 OBSERVATIONS AND DATA REDUCTION

Ultraviolet (UV), optical, and near-infrared (NIR) photometric and spectroscopic observations of LSQ13ddu were obtained at a number of facilities detailed below. These observations span from very soon after explosion out to a few months after maximum light when LSQ13ddu had faded below the detection limit of available instrumentation. All reduced data will be available through the WISeREP archive (Yaron & Gal-Yam 2012).[2]

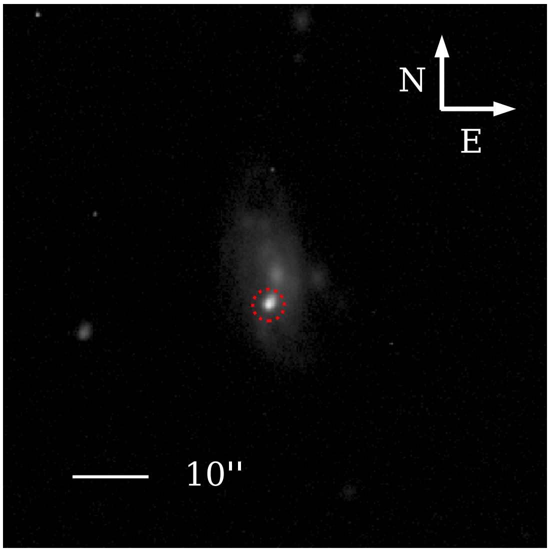

Figure 1. NTT EFOSC2 *V*-band image obtained on MJD 56626.1 with LSQ13ddu marked by the red circle.

2.1 Optical photometry

LSQ13ddu was discovered by LSQ on 2013 November 25, Modified Julian Date (MJD) of 56623.3, in the broad $g + r$ search filter, *LSQgr* (e.g. Baltay et al. 2013). The *LSQgr* light curve of LSQ13ddu covers from the time of discovery until ∼40 d after peak. The *LSQgr* data were reduced following the method described in Scalzo et al. (2014), making use of stars in the field of the SN calibrated to the AAVSO All-Sky Photometric Survey (APASS) catalogue (Henden et al. 2009). A non-detection at the position of LSQ13ddu on MJD 56620.3 (2 d prior to the first detection) gives a 3σ apparent limiting *LSQgr*-band magnitude of 21.84. The *LSQgr* light curve of LSQ13ddu is presented in Fig. 2.

Multicolour photometry was obtained using a number of facilities: the Las Cumbres Observatory (LCOGT) 1-m robotic telescope network with the SBIG instrument, the LCOGT 2-m robotic telescopes with the Spectral camera (Brown et al. 2013), the European Southern Observatory (ESO) New Technology Telescope (NTT) using the EFOSC2 instrument (Buzzoni et al. 1984), and the Liverpool Telescope (LT) using the IO:O instrument (Steele et al. 2004). Additional follow-up was conducted as part of the Carnegie Supernova Project-II (CSP-II; Phillips et al. 2019) using the Henrietta Swope Telescope (Swope; Perez et al. 2012). The LSQ, LCOGT, LT, NTT, and Swope optical photometry is presented in Table 1 and in Fig. 3.

The LCOGT *BVgri* photometry was processed using the ORAC-DR pipeline (Jenness & Economou 2015). After undergoing pre-processing using the BANZAI pipeline (McCully et al. 2018) and image subtraction using the routine HOTPANTS[3] (Becker 2015), which is an implementation of the image subtraction routine described in Alard & Lupton (1997), the source was extracted using LCOGTSNPIPE (Valenti et al. 2016) with the resulting magnitudes

---

[1] Retrieved from the NASA/IPAC Extragalactic Database (NED).

[2] The WISeREP archive is accessible at https://wiserep.weizmann.ac.il/

[3] This routine is available from https://github.com/acbecker/hotpants

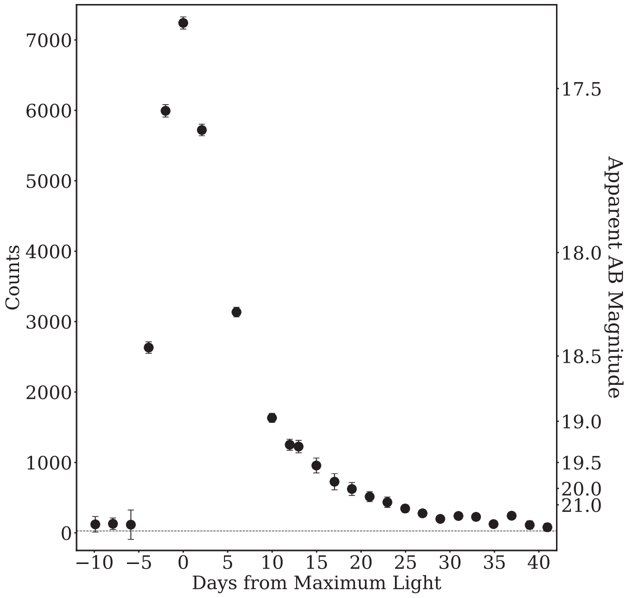

Figure 2. *LSQgr*-band observer frame light curve of LSQ13ddu, with the uncertainties generally smaller than the data point size.

calibrated using the APASS catalogue. The *BV* data and *gri* data were calibrated to Vega and AB magnitudes, respectively.

The LT *griz*-band photometry was measured on pre-processed imaging using a custom pipeline that includes subtraction of a reference template obtained at late times and calibration to the Pan-STARRS magnitude system, which is close to the AB system.

The *V*-band images obtained using the NTT were processed using the PESSTO photometric pipeline (Smartt et al. 2014), followed by image subtraction using HOTPANTS and NTT images obtained of the field taken after the SN had faded with calibration using the APASS catalogue in Vega magnitudes. The photometry was measured using the SNOOPY[4] software.

Two epochs of Swope *BVri* data were reduced in the manner outlined in Phillips et al. (2019) including image subtraction, with these observations calibrated to the Vega magnitude system.

2.2 UV and NIR photometry

Several epochs of *Swift* UVOT data spanning from +4.8 to +10.8 d post *LSQgr* maximum light were obtained. These data were retrieved from the Swift Optical/Ultraviolet Supernova Archive (SOUSA) and were processed using the method outlined in Brown et al. (2014), which includes subtraction for the underlying host flux.

A single epoch of pre-maximum *YJH* photometry was obtained with the Irénée du Pont 2.5-m telescope using the RetroCam instrument (du Pont + RetroCam; Hamuy et al. 2006). This photometry was reduced in the manner outlined in Phillips et al. (2019) including the subtraction of the underlying host galaxy using reference images.

Two epochs of NIR *JHK* photometry were obtained at the ESO NTT telescope with the SOFI instrument (Moorwood, Cuby & Lidman 1998). We performed image subtraction using a late-time image of the field and HOTPANTS. The reduction of the SOFI photometry was performed using IRAF and SNOOPY. The UV and NIR photometry of LSQ13ddu are presented in Tables 2 and 3, respectively, and are included with the optical light curves in Fig. 3.

2.3 Optical and NIR spectroscopy

Optical spectroscopy was obtained using the NTT with EFOSC2, the VLT with XShooter (Vernet et al. 2011), the LCOGT 2-m with FLOYDS,[5] WiFeS at the ANU 2.3-m (Dopita et al. 2007), and with the IMACS f/4 camera mounted on the Magellan–Baade telescope (Dressler et al. 2011). The spectroscopic data span from maximum light to +31 d post maximum. The details of these spectra are provided in Table 4. The EFOSC2 spectra were reduced using a custom pipeline, applying bias-subtraction, flat-fielding, wavelength and flux calibration, and a telluric correction was applied as described in Smartt et al. (2014). The XShooter spectrum was taken using 1.0, 0.9, and 0.9 arcsec wide slits in the UVB, VIS, and NIR arms, respectively. It was reduced in the standard manner using the ESO Reflex pipeline (Freudling et al. 2013). Telluric corrections were applied to the XShooter VIS arm using the MOLECFIT software (Kausch et al. 2015; Smette et al. 2015), but not to the NIR arm due to its lower signal to noise. The WiFeS spectra were obtained as part of the ANU WiFeS Supernova Programme (AWSNAP) with the reduction outlined in Childress et al. (2016). The IMACS spectrum was reduced using the COSMOS software package (Dressler et al. 2011; Oemler et al. 2017). The FLOYDS spectra were reduced using a custom pipeline. A telluric correction was applied to the IMACS and FLOYDS spectra following the method used for the EFOSC2 spectra. Two NIR spectra were obtained with Magellan + FIRE (Simcoe et al. 2013) and were reduced following the method described in Hsiao et al. (2019) using the tailored pipeline FIREHOSE (Simcoe et al. 2013). An absolute flux calibration was applied using coeval photometric data.

The spectra have been corrected for Milky Way extinction using the Fitzpatrick (1999) law and an $E(B-V)$ value of 0.008 mag from Schlafly & Finkbeiner (2011) retrieved from NED. The spectra were corrected to the rest frame using a value of $z = 0.057787$, measured using host H α, H β, N II 6548, 6583, O III 5007, and S II 6717 Å lines in the XShooter and WiFeS spectra. The optical and NIR spectral sequences are presented in Figs 4 and 5, respectively.

3 ANALYSIS

In this section, we analyse the light curves of LSQ13ddu, construct a bolometric light curve, estimate the blackbody temperatures, and measure the evolution of the main spectral features. We also summarize the host galaxy properties. The use of SYNAPPS for spectral line identification is described, as well as potential light-curve powering mechanisms for LSQ13ddu using photometric modelling.

3.1 Light-curve parameters

Using a cubic spline fit to the peak data of the *LSQgr* band light curve, we obtained a date of maximum light of 56626.0 ± 0.2 MJD and apparent peak magnitude of 17.36 ± 0.02 mag with the peak absolute *LSQgr* magnitude found to be −19.70 ± 0.02 mag. A cubic spline fit to the early light curve constrains the rise time to peak brightness to be 4.8 ± 0.9 d with an explosion

---

[4] SNOOPY is a SN photometry package developed by E. Cappellaro.

[5] https://lco.global/observatory/instruments/floyds

Table 1. Summary of the optical photometry collected for LSQ13ddu, with *BVgri* from LCOGT, *LSQgr* from La Silla-QUEST, *V* from NTT, *BVri* from Swope, and *griz* photometry from the LT. Photometric detections at $<3\sigma$ are given as upper limits. Photometry is presented in the observer frame with no applied extinction corrections.

MJD	Date	Phase (d)[a]	*B* (mag)	*V* (mag)	*g* (mag)	*LSQgr* (mag)	*r* (mag)	*i* (mag)	*z* (mag)	Source
56616.3	2013 Nov 19	−9.7	–	–	–	>21.79	–	–	–	LSQ
56618.3	2013 Nov 21	−7.7	–	–	–	>21.72	–	–	–	LSQ
56620.3	2013 Nov 23	−5.7	–	–	–	>21.84	–	–	–	LSQ
56622.3	2013 Nov 25	−3.7	–	–	–	18.45 ± 0.03	–	–	–	LSQ
56624.2	2013 Nov 27	−1.8	17.47 ± 0.01	17.58 ± 0.01	–	17.56 ± 0.02	17.74 ± 0.01	17.99 ± 0.02	–	LSQ, Swope
56625.2	2013 Nov 28	−0.8	17.30 ± 0.02	17.36 ± 0.02	–	–	17.38 ± 0.01	17.74 ± 0.02	–	Swope
56626.1	2013 Nov 29	+0.1	–	17.45 ± 0.25	–	–	–	–	–	NTT
56626.2	2013 Nov 29	+0.2	–	–	–	17.35 ± 0.01	–	–	–	LSQ
56628.3	2013 Dec 01	+2.3	–	–	–	17.61 ± 0.02	–	–	–	LSQ
56629.3	2013 Dec 02	+3.3	–	17.74 ± 0.27	–	–	–	–	–	NTT
56632.0	2013 Dec 05	+6.0	18.34 ± 0.04	18.15 ± 0.04	18.22 ± 0.02	–	–	–	–	LCOGT
56632.1	2013 Dec 05	+6.1	18.47 ± 0.06	18.27 ± 0.03	–	–	–	–	–	LCOGT
56632.2	2013 Dec 05	+6.2	–	–	–	18.26 ± 0.02	18.30 ± 0.04	18.39 ± 0.06	–	LCOGT, LSQ
56632.3	2013 Dec 05	+6.3	18.57 ± 0.04	18.21 ± 0.02	18.23 ± 0.03	–	–	–	–	LCOGT
56633.1	2013 Dec 06	+7.1	–	18.43 ± 0.02	–	–	–	–	–	LCOGT
56633.6	2013 Dec 06	+7.6	18.79 ± 0.07	18.43 ± 0.04	18.45 ± 0.02	–	–	–	–	LCOGT
56636.2	2013 Dec 09	+10.2	–	–	–	18.97 ± 0.04	–	–	–	LSQ
56636.5	2013 Dec 09	+10.5	19.43 ± 0.11	18.88 ± 0.09	–	–	18.85 ± 0.07	18.58 ± 0.06	–	LCOGT
56636.6	2013 Dec 09	+10.6	–	–	19.00 ± 0.05	–	–	18.85 ± 0.12	–	LCOGT
56638.2	2013 Dec 11	+12.2	–	–	–	19.26 ± 0.07	–	–	–	LSQ
56638.3	2013 Dec 11	+12.3	–	19.23 ± 0.07	19.31 ± 0.05	–	19.43 ± 0.08	19.53 ± 0.14	–	LCOGT
56639.2	2013 Dec 12	+13.2	–	–	–	19.28 ± 0.08	–	–	–	LSQ
56639.3	2013 Dec 12	+13.3	19.97 ± 0.18	19.32 ± 0.08	19.35 ± 0.06	–	19.42 ± 0.08	–	–	LCOGT
56640.2	2013 Dec 13	+14.2	–	–	19.65 ± 0.06	–	19.44 ± 0.12	19.78 ± 0.23	–	LCOGT
56641.2	2013 Dec 14	+15.2	–	–	–	19.55 ± 0.12	–	–	–	LSQ
56642.9	2013 Dec 16	+16.9	–	–	19.79 ± 0.11	–	19.86 ± 0.12	20.26 ± 0.16	19.75 ± 0.12	LT
56643.2	2013 Dec 16	+17.2	–	–	–	19.85 ± 0.17	–	–	–	LSQ
56643.9	2013 Dec 17	+17.9	–	–	19.93 ± 0.10	–	19.90 ± 0.08	20.01 ± 0.09	19.60 ± 0.06	LT
56644.7	2013 Dec 18	+18.7	20.02 ± 0.30	19.39 ± 0.30	20.02 ± 0.16	–	20.12 ± 0.15	20.31 ± 0.21	–	LCOGT
56644.9	2013 Dec 18	+18.9	–	–	–	–	19.87 ± 0.09	20.19 ± 0.11	19.82 ± 0.11	LT
56645.1	2013 Dec 18	+19.1	–	–	–	20.04 ± 0.17	–	–	–	LSQ
56645.9	2013 Dec 19	+19.9	–	–	19.85 ± 0.09	–	20.07 ± 0.12	20.04 ± 0.11	19.74 ± 0.12	LT
56646.7	2013 Dec 20	+20.7	–	–	–	–	20.35 ± 0.20	20.68 ± 0.30	–	LCOGT
56646.9	2013 Dec 20	+20.9	–	–	20.02 ± 0.06	–	20.09 ± 0.08	20.44 ± 0.09	19.80 ± 0.07	LT
56647.1	2013 Dec 20	+21.1	–	–	–	20.23 ± 0.15	–	–	–	LSQ
56648.5	2013 Dec 21	+22.5	20.64 ± 0.13	–	20.27 ± 0.16	–	20.75 ± 0.27	21.02 ± 0.33	–	LCOGT
56648.9	2013 Dec 22	+22.9	–	–	20.37 ± 0.05	–	–	20.88 ± 0.13	20.02 ± 0.08	LT
56649.1	2013 Dec 22	+23.1	–	–	–	20.43 ± 0.17	–	–	–	LSQ
56649.9	2013 Dec 23	+23.9	–	–	–	–	–	–	20.16 ± 0.08	LT
56650.9	2013 Dec 24	+24.9	–	–	20.50 ± 0.04	–	20.80 ± 0.06	20.76 ± 0.07	–	LT
56651.1	2013 Dec 24	+25.1	–	–	–	20.70 ± 0.18	–	–	–	LSQ
56651.9	2013 Dec 25	+25.9	–	–	20.58 ± 0.03	–	20.75 ± 0.08	20.94 ± 0.09	20.17 ± 0.10	LT
56652.5	2013 Dec 25	+26.5	21.51 ± 0.45	20.41 ± 0.50	–	–	20.83 ± 0.14	–	–	LCOGT
56653.1	2013 Dec 26	+27.1	–	–	–	20.89 ± 0.13	–	–	–	LSQ
56654.4	2013 Dec 27	+28.4	–	–	–	–	21.20 ± 0.37	–	–	LCOGT
56654.5	2013 Dec 27	+28.5	–	20.49 ± 0.38	–	–	–	21.44 ± 0.36	–	LCOGT
56655.1	2013 Dec 28	+29.1	–	–	–	21.26 ± 0.19	–	–	–	LSQ
56656.4	2013 Dec 29	+30.4	–	–	–	–	21.18 ± 0.50	21.63 ± 0.46	–	LCOGT
56656.5	2013 Dec 29	+30.5	–	20.86 ± 0.41	–	–	–	–	–	LCOGT
56657.1	2013 Dec 30	+31.1	–	–	–	21.07 ± 0.23	–	–	–	LSQ
56658.9	2014 Jan 01	+32.9	–	–	20.94 ± 0.06	–	21.30 ± 0.09	21.49 ± 0.13	20.81 ± 0.29	LT
56659.1	2014 Jan 01	+33.1	–	–	–	20.96 ± 0.15	–	–	–	LSQ
56661.1	2014 Jan 03	+35.1	–	–	–	>21.76	–	–	–	LSQ
56663.1	2014 Jan 05	+37.1	–	–	–	21.03 ± 0.17	–	–	–	LSQ
56665.2	2014 Jan 07	+39.2	–	–	–	>21.88	–	–	–	LSQ
56667.1	2014 Jan 09	+41.1	–	–	–	>22.25	–	–	–	LSQ
56668.8	2014 Jan 11	+42.8	–	–	21.71 ± 0.31	–	21.57 ± 0.60	21.69 ± 0.32	–	LT

[a] Phase is relative to maximum light in the *LSQgr* band: 17.35 ± 0.01 on MJD 56626.2.

epoch of 56620.9 ± 0.7 MJD, consistent with the deep *LSQgr* non-detection at -5.7 d prior to peak. During its rise to peak, LSQ13ddu brightened at a rate of $\sim$0.75 mag d^{-1} with a $\Delta m_{15}(LSQgr)$ of 2.20 ± 0.14 mag giving a decline rate of 0.15 ± 0.01 mag d^{-1} in the *LSQgr* band over the first 15 d post maximum light.

3.1.1 *Pseudo-bolometric light curve*

We computed two pseudo-bolometric light curves for LSQ13ddu using the python code, SUPERBOL (Nicholl 2018). One using the data from the optical ($B \rightarrow i$) bands to serve as a comparison with literature objects and as an input for photometric modelling using the light-curve fitting code MOSFIT (Guillochon et al. 2018) (see Section 3.5). The second bolometric light curve calculated includes the early-time *Swift* UV data and an extrapolation assuming a single temperature blackbody to account for non-observed bands. This 'full' bolometric curve spans the range 1000–25 000 Å and is used to constrain the total peak luminosity. In both cases, we chose the band with the most consistent coverage, *LSQgr*, as the reference filter. The other filters are interpolated to the epochs of *LSQgr* data

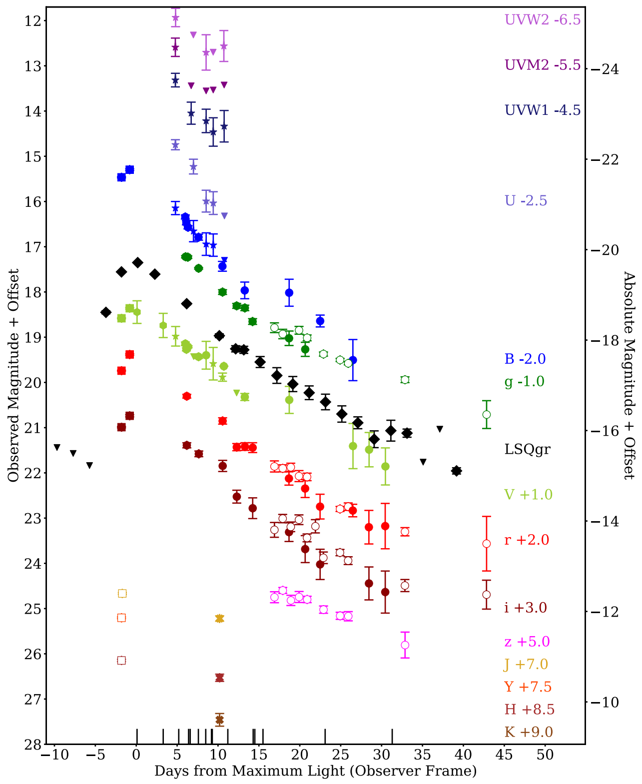

Figure 3. UV, optical, and NIR light curves of LSQ13ddu in observed and absolute magnitudes with the different instruments shown as follows: *Swift* UV (stars), LCOGT optical (filled circles), LT optical (open circles), LSQ optical (filled diamonds), Swope optical (filled squares), NTT optical (hexagons), du Pont NIR (open squares), and NTT NIR (crosses). Data points have the offsets applied as specified in the legend. The late-time NTT NIR data are excluded for plotting purposes. Upper limits are displayed as downward facing triangles. The phases of the spectral observations are indicated with tick marks along the bottom axis.

using a polynomial with the photometric uncertainties providing a weighting for the fits. At phases prior to or after the availability of multiband photometry, constant colour approximations are used.

The use of the optical pseudo-bolometric light curve is twofold. First, literature objects do not typically have as extensive a photometric data set as LSQ13ddu, with UV photometry not routinely obtained. Secondly, UV data are only available for LSQ13ddu at early times with the constant colour approximation significantly overestimating the UV contribution to the overall luminosity at late times. The LT *z* band, RetroCam, and SOFI NIR data have been excluded due to lack of consistent coverage and/or insufficient sampling.

The peak luminosity of the pseudo-bolometric light curves are after accounting for extinction $2.81 \pm 0.26 \times 10^{43}$ erg s^{-1} for the 'full' version and $1.03 \pm 0.11 \times 10^{43}$ erg s^{-1} for the optical version. Optical pseudo-bolometric light curves of a sample of SNe Ibn (SN 2011hw; Smith et al. 2012, LSQ13ccw; Pastorello et al. 2015c, SN 2014av; Pastorello et al. 2016 and SN 2010al; Pastorello et al. 2015a) were computed in a similar manner and are compared to that of LSQ13ddu in Fig. 6. The behaviour of the optical bolometric light curve of LSQ13ddu is found to match that of SN 2014av, with SN 2014av having a peak luminosity of $8.49 \pm 0.82 \times 10^{42}$ erg s^{-1} along with very similar pre- and post-maximum light-curve evolution.

3.2 Blackbody temperature and colour evolution

The blackbody temperature of LSQ13ddu was estimated using a single temperature fit to both the spectroscopic and photometric data. The assumption is that the ejecta is a uniform temperature and lacks additional components from other effects such as dust re-radiating at redder wavelengths. In the spectral analysis, we measured the temperature using a least-squares fit to each spectrum using the SCIPY curve fitting routine (Jones et al. 2001). The spectra have not undergone additional processing (e.g. no emission or absorption features have been removed prior to fitting) with the exception of the removal of the high noise regions at the edges of several spectra. As a consistency check, the blackbody temperature was also calculated using the available multiband photometry at the same epochs as the spectra where there is sufficient multiband observations (≥4 bands) to produce a cubic spline interpolation to the photometry for fitting.

The earliest spectra (+0.1 and +3.3 d) are relatively featureless and are well fitted by the blackbody model, with an initial temperature of 13 000 ± 500 K at +0.1 d, cooling to 11 300 ± 500 K at +3.3 d. At epochs after ∼3 d post maximum, the spectra of LSQ13ddu start to show stronger spectral features that deviate from the underlying blue continuum and make fitting a blackbody to the data more difficult. However, we measured a general cooling with time with the ejecta reaching a blackbody temperature of ∼7000 K at +6–8 d past maximum. The values obtained using both the spectra and multiband photometry show good agreement.

While the continued strengthening of broad spectral features prevents the determination of a reliable blackbody temperatures at later phases, colour measurements using photometric data can provide some insight into the continued temperature evolution of LSQ13ddu. Fig. 7 is a comparison between the colour evolution of LSQ13ddu, the SNe Ibn, SN 2006jc (Pastorello et al. 2007), SN 2010al (Pastorello et al. 2015a), and SN 2014av (Pastorello et al. 2016), along with the normal Type Ic SN 2007gr (Hunter et al. 2009). From this comparison the observed colour evolution of LSQ13ddu is found to be similar to that of SN 2010al and SN 2014av, with all three being redder than SN 2006jc but significantly bluer than the normal Type Ic SN 2007gr at similar phases.

3.3 Spectroscopic analysis

The features in the spectra of LSQ13ddu are analysed using the spectral fitting code SYNAPPS (Thomas, Nugent & Meza 2011). Velocity measurements of the main features (both the narrow He and broader underlying features) are also analysed using Gaussian fits to the lines. The contamination of SN spectral features by narrow host galaxy emission lines, as well as the properties of the host, are also discussed.

3.3.1 Host galaxy properties and line contamination

Due to its location within its host, the spectra of LSQ13ddu show contamination from narrow host emission lines. As the CSM signatures are narrow and weak, care must be taken to disentangle the host contamination from potential SN-related features. Their relative contributions were determined in three ways: (i) a line velocity analysis and (ii) a spectral comparison between the host and LSQ13ddu using multiple extractions of the 2D spectra, and (iii) a comparison between the H *α* and N II 6583 Å features.

First, we measured the full width half-maximum (FWHM) velocity of the host galaxy emission lines using Gaussian fits

Table 2. Summary of the *Swift* UVOT photometry, with detections at $<3\sigma$ given as upper limits.

MJD	Date	Phase (d)[a]	*UVW2* (mag)	*UVM2* (mag)	*UVW1* (mag)	*U* (mag)	*B* (mag)	*V* (mag)
56630.8	2013 Dec 04	+4.8	18.43 ± 0.20	18.09 ± 0.20	17.82 ± 0.15	17.25 ± 0.11	18.15 ± 0.15	17.98 ± 0.22
56632.7	2013 Dec 06	+6.7	–	>18.94	18.55 ± 0.24	–	–	–
56633.0	2013 Dec 06	+7.0	>18.82	–	–	17.73 ± 0.16	18.66 ± 0.24	>18.43
56634.5	2013 Dec 07	+8.5	19.20 ± 0.39	>19.06	18.72 ± 0.26	–	–	18.40 ± 0.31
56634.6	2013 Dec 07	+8.6	–	–	–	18.49 ± 0.24	18.94 ± 0.25	–
56635.4	2013 Dec 08	+9.4	>19.20	>19.04	18.96 ± 0.31	18.54 ± 0.25	18.96 ± 0.25	18.69 ± 0.36
56636.7	2013 Dec 10	+10.7	19.06 ± 0.34	>18.93	–	–	–	>18.64
56636.8	2013 Dec 10	+10.8	–	–	18.84 ± 0.35	>18.82	>19.30	–

[a] Phase is relative to maximum light in the *LSQgr* band in the observed frame.

Table 3. Details of the NIR photometry of LSQ13ddu.

MJD	Date	Phase (d)[a]	Magnitude	Band	Source
56624.2	2013 Nov 27	− 1.8	17.70 ± 0.02	*Y*	(1)
56624.2	2013 Nov 27	− 1.8	17.65 ± 0.03	*H*	(1)
56624.3	2013 Nov 27	− 1.7	17.67 ± 0.02	*J*	(1)
56636.2	2013 Dec 09	+10.2	18.22 ± 0.06	*J*	(2)
56636.2	2013 Dec 09	+10.2	18.03 ± 0.08	*H*	(2)
56636.2	2013 Dec 09	+10.2	18.46 ± 0.14	*K*	(2)
56695.1	2014 Feb 06	+69.1	21.34 ± 0.38	*J*	(2)
56695.1	2014 Feb 06	+69.1	20.65 ± 0.35	*H*	(2)

Notes. (1) du Pont+RetroCam, (2) NTT + SOFI

[a] Phase is relative to maximum light in the *LSQgr* band in the observed frame.

in one of our highest resolution spectra obtained with XShooter, which has a velocity resolution of $\sim$35 km s^{-1} (measured from sky lines). The FWHM velocity of the H α feature was measured to be 260 ± 40 km s^{-1}, which was consistent with the widths of the nebular emission lines (not typically seen in SN spectra) of 220 ± 50, 250 ± 40, and 180 ± 40 km s^{-1} for the N II 6548 Å, N II 6583 Å, and S II 6715 Å lines, respectively.

Secondly, to determine if there is a contribution from CSM associated with the SN to the narrow H α signature, extractions from stare-mode 2D spectra were made at three locations along the slit as shown in Fig. 8: (i) at the SN location, (ii) at a position offset but close to the SN, and (iii) at the nucleus of the host galaxy. As the extended emission from the host spans the full frame, clean sky subtraction was difficult and to remove the possibility of introducing artefacts into the spectra was not attempted. The location of the sky lines have been marked in both the 1D and 2D spectra using black ticks. For the H α region, a velocity gradient is seen across the slit with the peak of the H α emission of the nucleus offset from the SN position by $\sim$200–250 km s^{-1}(no such feature is visible at the He I lines). The H α and N II 6583 Å emission features at the offset position close to the SN and at the location of the SN are well matched in both width and strength.

Thirdly, we estimated the size of the potential SN contribution to the H α feature by subtracting a Gaussian with a width equivalent to the measured FWHM of the host galaxy N II 6583Å line from the H α feature of the NOD mode + 5 d XShooter spectrum. When the Gaussian estimates of the contribution from the host galaxy are subtracted off, there is a residual flux of 14 ± 14 percent (using the uncertainties on the measured FWHM), which within the uncertainties is consistent with zero, suggesting little or no SN contribution to the H α feature.

Taken together, the consistent line widths and strengths at the location of LSQ13ddu compared to the offset positions shows that the narrow emission feature of H α is dominated by host light and does not appear to be intrinsic to the environment of LSQ13ddu, although a small contribution of up to $\sim$14 percent cannot be ruled out.

Fig. 8 also includes the corresponding 1D and 2D frames at the locations of the He I 3889 Å and He I 6678 Å lines (features from the UVB and VIS XShooter arms, respectively). The He I features are seen as weak P-Cygni profiles at the SN position of both lines but are not seen at the positions of the host nucleus or the offset position from the SN.

The local metallicity of the host galaxy at the location of LSQ13ddu was estimated from measurements of the line strength ratios of key galaxy emission lines in the +15 d WiFeS spectrum. The gas-phase metallicity, 12 + log([O III]/H), of the host galaxy was calculated to be 8.51 ± 0.25 based on the O3N2 conversion ratio from Pettini & Pagel (2004). This value is equivalent to $\sim$0.7 times the solar metallicity value of Asplund et al. (2009) and is consistent with previous metallicity studies of SNe Ibn that find sub-solar host metallicities for the class (Pastorello et al. 2015a; Taddia et al. 2015). Additionally, an archival 6DF spectrum (Jones et al. 2009) of the nuclear region of the host of LSQ13ddu was used to identify any active galactic nucleus (AGN) activity. From this spectrum a log([N III/H α]) value of −0.425 and a log([O III/H β]) value of −0.177 were estimated, placing the host below both the Kewley theoretical dividing line (Kewley et al. 2001) and the Kauffmann SDSS based empirical dividing line (Kauffmann et al. 2003) on the 'Baldwin, Phillips & Terlevich' (BPT) diagram (Baldwin, Phillips & Terlevich 1981), we thus conclude that the galaxy is not the host of an AGN and has the properties of a star-forming galaxy.

3.3.2 *Presence of narrow P-Cygni features*

We investigated the presence of the weak and narrow He-related features in the spectra of LSQ13ddu. Fig. 9 shows the time evolution from 0 to +5 d of the narrow P-Cygni features that are visible in the early optical spectra. A P-Cygni feature initially linked to *He ii* 4686 Å but as discussed below, more likely a blend of C and N, was clearly detected in the earliest spectrum of LSQ13ddu at +0.1 d (left-hand panel). This is the only clear feature identified in the maximum light spectrum and is no longer visible at +3.3 d. Features similar to this have previously been identified in SN 2010al (Pastorello et al. 2015a) and tentatively in SN 2014av (Pastorello et al. 2016). In particular, the feature in the earliest two spectra obtained of SN 2010al initially presented as a double-peaked emission feature before transitioning to two distinct P-Cygni profiled absorption lines by six days after maximum, before disappearing by 15 d after maximum light. This feature was identified as a combination of the He II 4686 Å line, responsible for the redder peak, and a blended C III 4648 Å + N III 4640 Å

Table 4. Log of the spectroscopic observations of LSQ13ddu presented in this paper.

MJD	Date	Phase (d)	Telescope	Instrument	Configuration	Wavelength range (Å)[a]	Resolution (λ/Δλ)[b]
56626.1	2013 Nov 29	+0.1	NTT	EFOSC2	GR13	3460–8760	310
56629.3	2013 Dec 02	+3.3	NTT	EFOSC2	GR11	3170–7070	280
56631.2	2013 Dec 04	+5.2	VLT	XShooter	UV, VIS, NIR[c]	2970–22 500	5400 8820 5600
56632.6	2013 Dec 05	+6.4	ANU 2.3m	WiFeS	B, R	3310–9040	4430 2350
56632.6	2013 Dec 05	+6.6	Las Cumbres	FLOYDS	–	3060–9450	470 380
56633.6	2013 Dec 06	+7.6	Las Cumbres	FLOYDS	–	3030–10 000	470 350
56634.5	2013 Dec 07	+8.5	Las Cumbres	FLOYDS	–	3030–10 000	280 230
56635.2	2013 Dec 08	+9.2	NTT	EFOSC2	GR11, GR16 OG530	3180–9450	390 440
56635.3	2013 Dec 08	+9.3	Magellan Baade	FIRE	Longslit	7650–22 500	400
56137.2	2013 Dec 10	+11.2	NTT	EFOSC2	GR11, GR16 OG530	3170–9450	400 430
56640.3	2013 Dec 13	+14.3	Magellan Baade	FIRE	Longslit	7650–22 500	400
56640.5	2013 Dec 13	+14.5	Las Cumbres	FLOYDS	Red	4500–9600	200
56641.5	2013 Dec 14	+15.5	ANU 2.3m	WiFeS	B, R	3310–9040	4220 2380
56649.1	2013 Dec 22	+23.1	NTT	EFOSC2	GR13	3470–8760	310
56657.3	2013 Dec 30	+31.3	Magellan Baade	IMACS–f/4	300	3400–9100	1300

[a] Wavelength ranges are given in the rest frame of the SN.

[b] The resolution is calculated where possible from the night sky lines or taken from the instrument specifications.

[c] UVB and VIS arms consisted of two 1300s exposures while due to an error the NIR arm was two 130s exposures resulting in low S/N in the NIR spectrum.

feature producing the bluer emission peak. The velocities of these features measured based on their absorption minima was found to be ∼1000 km s^{-1} consistent with measurements of He I P-Cygni absorption minima in the same spectrum at 1000–1100 km s^{-1}. The identification of He II in SN 2010al was confirmed through the detection of the He II 5411 and 8236 Å features that are not observed in LSQ13ddu.

The velocity of the absorption minimum of the feature in the first spectrum of LSQ13ddu was measured to be 2950 km s^{-1} if treated as He II 4686 Å 600 km s^{-1} if treated as C III 4648 Å, and 80 km s^{-1} if treated as N III, giving a mean C III + N III (i.e. 4644 Å) blend velocity of 340 km s^{-1} . We discuss the most likely identification of this feature below in the context of the He I line velocities.

In common with SNe Ibn, narrow He I features were clearly observed in multiple spectra of LSQ13ddu starting at +3 d after maximum light and continuing until ∼11 d with a decrease in strength with time, with these features appearing largely in absorption, with faint emission components observed in the higher resolution +5 d XShooter spectrum. Fig. 10 is a comparison between the behaviour of the He I lines in the spectra of LSQ13ddu and those in the spectra of SN 2010al and ASSASSN-15ed. The strongest (although still weak) features seen in LSQ13ddu are those of He I 3889, 4471, 5876, and 6678 Å). In the higher resolution XShooter and WiFeS spectra obtained at +5 and +6 d, respectively, weaker narrow He I features at 3889, 4922, 5016, and 7065 Å can also be identified. Marginal detections of He I 4471, 5016, and 5876 Å features are seen in the first spectrum of LSQ13ddu at velocities comparable to those seen in later spectra. However, as they are of low significance, they are excluded from further analysis.

The blueshifted absorption minimum velocities were estimated for the identified He I features and found to be in the range ∼90–1120 km s^{-1} (Fig. 11). The uncertainties on the velocities were estimated by taking the uncertainties on the fits added in quadrature to the uncertainties due to the spectral resolution. The highest resolution spectrum is the XShooter one at +5 d with a resolution of ∼35 km s^{-1}, while the lowest resolution obtained with EFOSC2 is ∼600 km s^{-1}, with the higher resolution spectra giving significantly lower absorption velocities.

To determine if differing spectral resolution is the main source of the variation in the measured velocities, we rebinned the XShooter spectrum to 3 Å to match our lower resolution spectra and remeasured the velocities of the He I features. When measured from the rebinned spectrum, the lines were found to be broadened significantly, the absorption velocities of the 4471 and 6678 Å lines increased from 250 ± 90 and 220 ± 90 km s^{-1} to 860 ± 200 and 850 ± 180 km s^{-1}, respectively. Additionally, the weaker feature at 7065 Å was no longer distinguishable in the spectrum. Therefore, we conclude the He I velocities are constant within the uncertainties in range of +3 to +11 d and using the highest resolution XShooter and WiFeS spectra, we obtain a weighted mean He I absorption minimum velocity of 250 ± 20 km s^{-1}, which we use hereafter as our preferred value. The velocity of He I features in SNe Ibn has been shown to display little evolution with time (Pastorello et al. 2016) and are typically higher than the values obtained for LSQ13ddu but this may be a consequence of the higher than normal resolution of our LSQ13ddu spectra compared to the literature sample.

If we assume that the material producing the He I features is also responsible for producing the features observed in the first spectrum of LSQ13ddu, then to obtain a consistent velocity, the first spectrum feature is most likely a blend of C III 4648 Å and N III 4640 Å at ∼340 km s^{-1}, and not He II 4686 Å. This is corroborated by the lack of detection of other He II lines, such as those at 5411 and 8236 Å. Although there is no detection of a narrow P-Cygni He I 10 830 Å feature in the +5 d spectrum of LSQ13ddu, a broad He I 10 830 Å emission feature is observed in the +9 and +14 d spectra and is discussed further in the context of the other broad spectral features in Section 3.3.3.

3.3.3 Spectral evolution of broad features and line identification

In addition to the narrow features seen in LSQ13ddu, a broad emission feature is visible in the range ∼3700–3900 Å in the first +0.1 d spectrum of LSQ13ddu (see Fig. 4). The identification of the elements producing these features is uncertain but this region typically contains Fe II lines (Pastorello et al. 2016). If this broad feature is taken to be a single feature, it displays a FWHM velocity

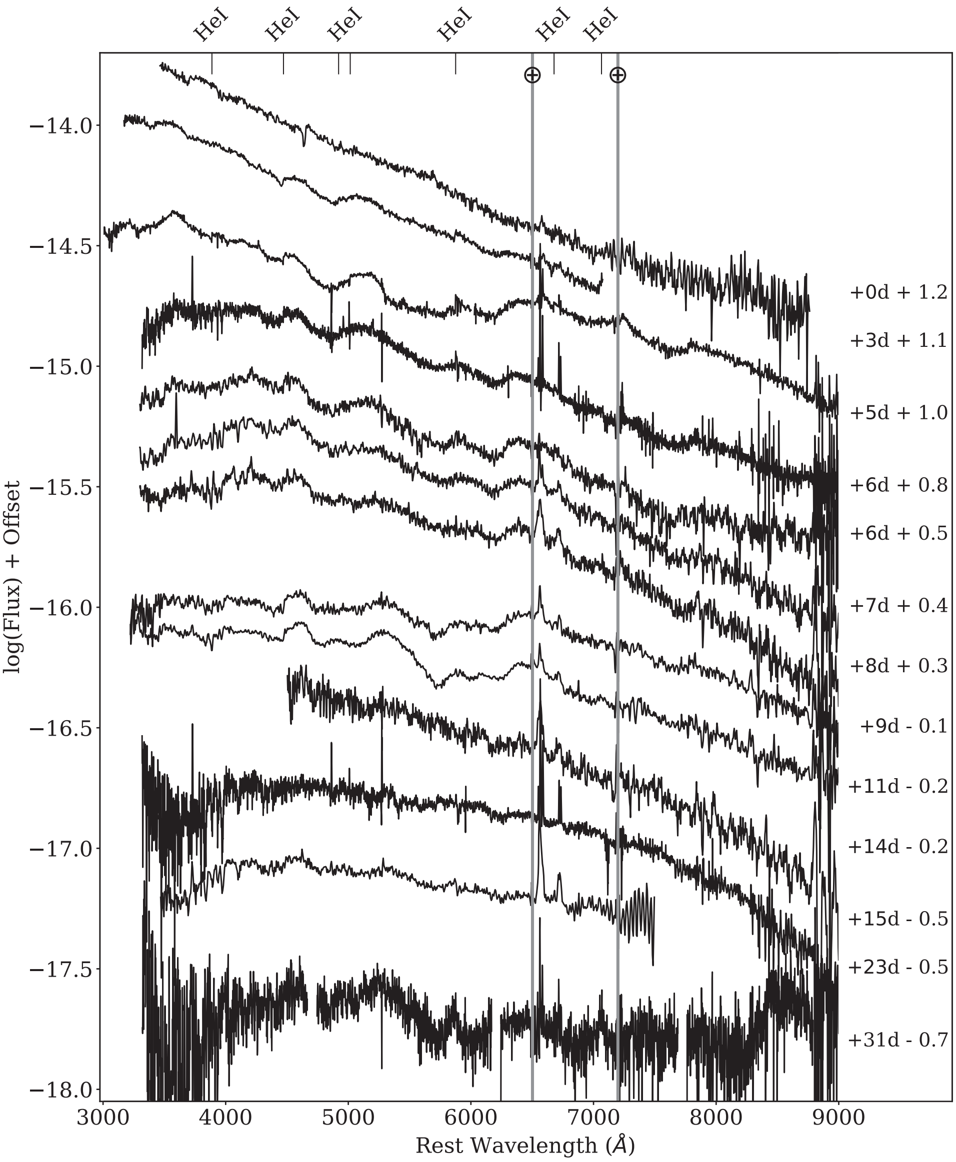

Figure 4. Optical spectral sequence of LSQ13ddu. The location of the He I line sequence is shown by the tick marks. The position of telluric regions are marked with cross hairs. For comparison with the lower resolution spectra, the XShooter spectrum at +5 d has undergone a 5σ clipping and been rebinned to 3 Å in this plot.

of 15 700 ± 2600 km s^{-1}, which is typical of early-phase SN ejecta. A similar feature was identified in a maximum-light spectrum of SN 2014av (and attributed to a Ca II H&K and He I line blend) but its peak was blueshifted by ∼6000 km s^{-1} with respect to that of LSQ13ddu. By the time of the second spectrum at +3 d, the broad feature at 3700–3900 Å has disappeared. New broad features have developed at 3350–3750, 4440–4700, and 4850–5300 Å, which are likely due to Fe II emission (Pastorello et al. 2016).

At later times (>+9 d), the spectra have evolved to become dominated by these broad features. We have used the spectral fitting code SYNAPPS described in Thomas et al. (2011) to the +9 d spectrum, to determine the elements contributing to the broad SN-like features that develop with time. SYNAPPS is based on the SYNOW fitting code (Fisher 2000) but instead of being interactive, it optimizes the input parameters to produce a best fit. SYNAPPS has the same assumptions and limitations of SYNOW and is best for line identification and rough estimates of the spectral velocities since it does not provide measures of the ionic species abundances and therefore cannot be used to infer the masses of the elements present in the ejecta.

Fig. 12 shows the SYNAPPS fits to the +9 d spectrum, along with the key features contributing to each line. The ions used in the fits are: C II, Ca II, Co II, Fe II, He I, N III, O I, and Si II. In particular, underlying broad He I is essential to fit the ∼5200–6000 and ∼6300–6600 Å regions. The velocities of these ions are 10 200 km s^{-1}. The presence of He II and H were checked for but neither provided a significant improvement to the fit and thus we cannot unambiguously identify their presence in the spectrum.

A broad He I 10 830 Å emission feature is observed in the +9 and +14 d spectra, with the strength of this feature seen to increase with time (Fig. 5). Its measured FWHM velocity is 9400 ± 700 and 10 200 ± 700 km s^{-1} at +9 and +14 d past maximum light, respectively, which are consistent within the uncertainties. The 10 830 Å feature at +9 d appears to be redshifted by ∼1200 km s^{-1}

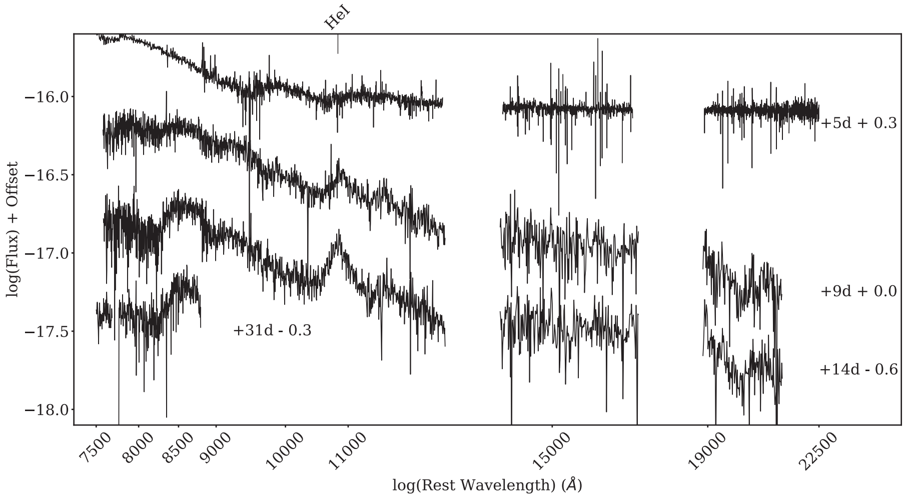

Figure 5. NIR spectral sequence of LSQ13ddu. The +31 d Magellan Baade IMACS optical spectrum is also partially included to highlight the evolution of the Ca II triplet region. The XShooter spectrum at +5 d has undergone a 5σ clipping procedure for display purposes. We note the low S/N of the XShooter NIR spectrum as a result of a short exposure time. Regions of significant telluric contamination across all spectra are not shown. The position of the strong He I 10 830 Å line is also indicated.

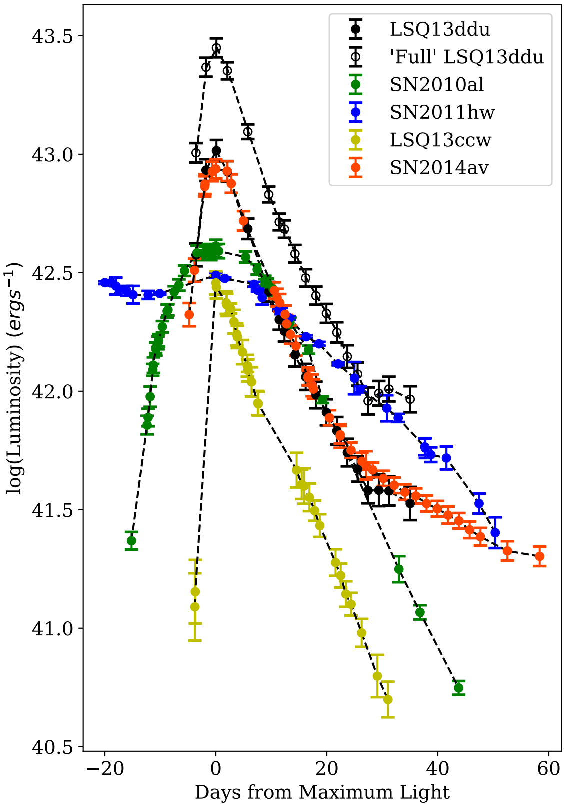

Figure 6. Pseudo-bolometric ($B \rightarrow i$) band light curve (solid black points) for LSQ13ddu compared to the light curves of a sample of SNe Ibn (detailed in the text). The 'full' bolometric light curve of LSQ13ddu is also shown in open black points. A time dilation correction to account for the redshift of the objects has been applied to the light curves.

with respect to its rest wavelength but the +14 d feature is consistent with no velocity offset. This could suggest a residual though unresolved narrow He I feature is causing the offset in the first spectrum and that is gone by the time of the later spectrum.

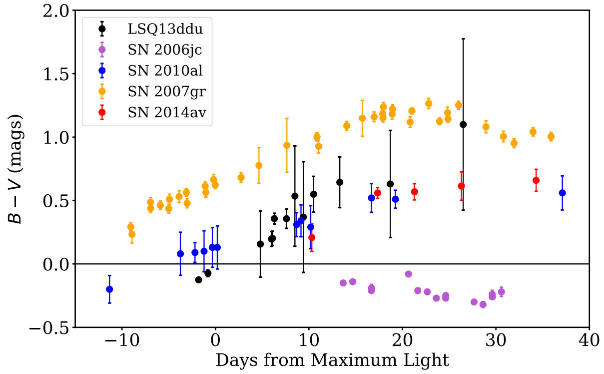

Figure 7. A comparison of the $B - V$ colour evolution of LSQ13ddu with SNe Ibn SN 2006jc (Pastorello et al. 2007), SN 2010al (Pastorello et al. 2015a), SN 2014av (Pastorello et al. 2016), and the Type SN Ic, SN 2007gr (Hunter et al. 2009).

The NIR Ca II triplet emission feature at 8200–9000 Å (which is likely blended with an O I line) first appears at +9 d and grows stronger with time. This evolution is clearly seen in the NIR spectra shown in Fig. 5. The strength of the potential Fe-group emission, at 9000–9550 Å and 11 300–11 900 Å and features due to O I and Mg II emission (7650–8100 Å) are also seen to grow with time. These broad features are similar to those seen in stripped-envelope SNe (SE-SNe) and are compared to a sample of them in Section 4.3.

3.4 Powering the light curve of LSQ13ddu

The rapid rise of LSQ13ddu to such a bright peak luminosity followed by a decay over a similar time-scale is difficult to achieve with a purely ^{56}Ni power source, with significant tension between the large ^{56}Ni mass required to produce such a bright event and its rapid photometric evolution (see Section 3.5.1). Studies of SNe Ibn have suggested that their light curves are likely powered by the decay of radioactive ^{56}Ni combined with an additional component from CSM interaction, i.e. as if they are CSM-enshrouded SE-SNe (e.g. Chugai 2009). Although the He-interaction features in

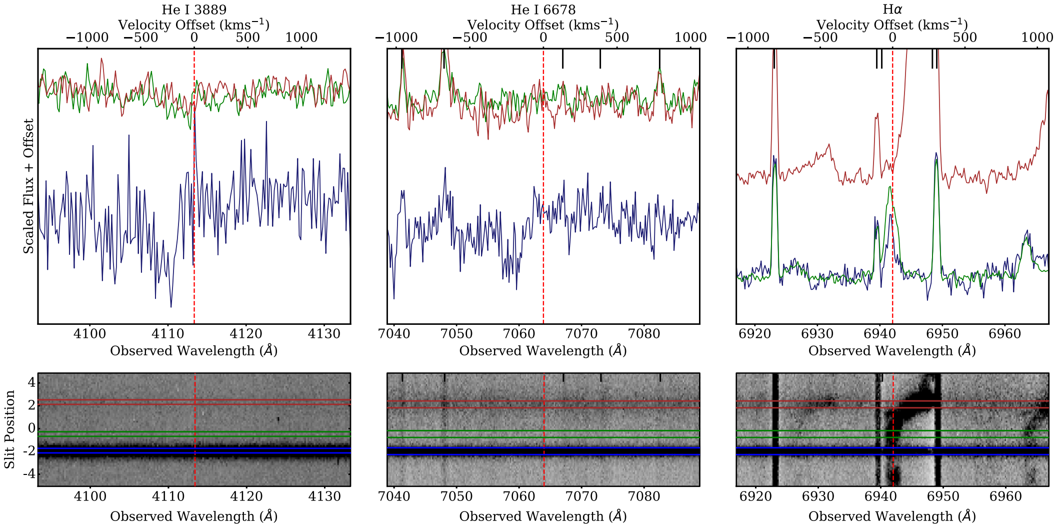

Figure 8. The upper panels show 1D spectral extractions at the position of the SN (blue), at a position close to the SN (green), and through the nucleus of the host galaxy (brown) in the observed wavelength range of He I 3889 Å (left), He I 6678 Å (middle), and H *α* (right). Zero-velocity is based on the SN position and labelled as a red dashed line. The He I SN spectrum is the median combination of both stare exposures. *Y*-axis offsets have been made for clarity. The corresponding regions in the 2D frames are displayed in the bottom panels with the same colour coding. Strong sky lines are indicated with short black ticks at the top of the plots. In the rightmost plots centred on the H *α* feature, the N II 6583 Å line is observed at a wavelength of 6963 Å at both the offset position close to the SN and at the SN position with both closely matched in their profile shape and strength.

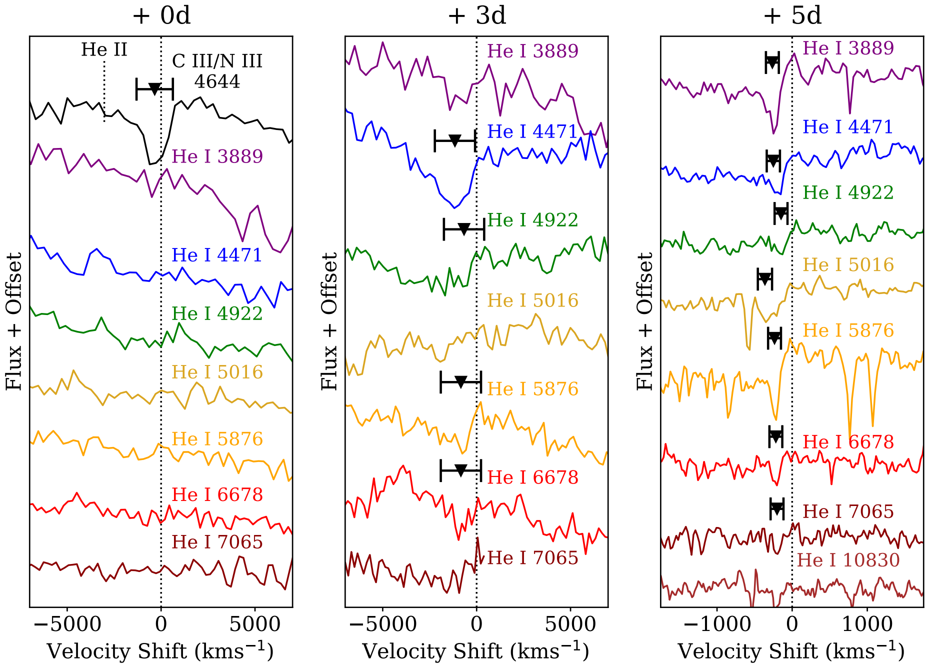

Figure 9. Spectral regions containing the strongest identified narrow He I features from 0 to +5 d after maximum light (left to right). Each feature displayed in velocity space relative to the rest location of the corresponding He I line. The absorption minima of detections are marked as solid downward facing triangles. The velocity of the blended C III + N III feature in the initial spectrum if treated as He II is also indicated as a short vertical dotted line.

LSQ13ddu are much weaker than in the SN Ibn sample studied to date, an additional (or alternative) powering source to ^{56}Ni decay is needed to explain its light-curve behaviour. A combined ^{56}Ni and CSM interaction model agrees qualitatively with the observed spectral evolution of LSQ13ddu, where narrow He features suggestive of CSM interaction are seen in the early spectra but fade away and become undetectable within a few weeks of maximum light.

To determine if LSQ13ddu could be powered by a combination of early-time CSM interaction and the ^{56}Ni decay of an underlying SE-SN light curve dominating at later times, we compared the bolometric light curve of LSQ13ddu with a light-curve sample of SE-SNe from Prentice et al. (2016). We identified a subset of objects with similar late-time photometric evolution to LSQ13ddu (left-hand panel of Fig. 13) and used them to determine an average SE-SN light-curve template. The sample used to produce this mean

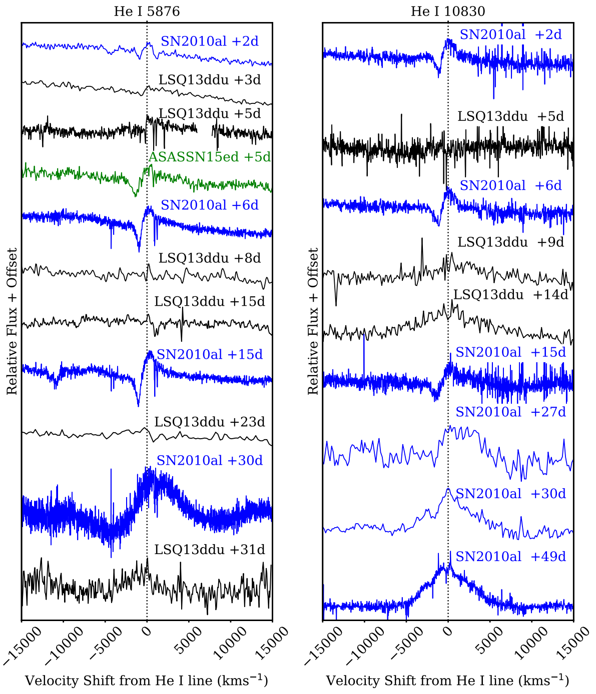

Figure 10. Comparison between the He I 5876 and 10 830 Å lines of LSQ13ddu (black), SN 2010al (blue), and ASSSN-15ed (green). Phases are from maximum light in the observer frame.

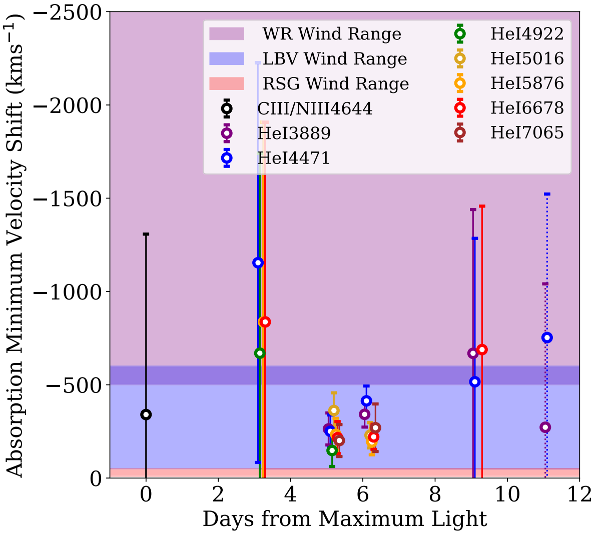

Figure 11. Velocity measurements of He I features observed in the spectra of LSQ13ddu along with the C III + N III blend observed in the first spectrum. Points with dashed error bars indicate features with uncertain identification due to lower signal-to-noise ratios. The expected range of WR wind speeds (500–3200 km s^{-1}) (Crowther 2007) is shown as the purple shaded region, the expected wind speeds of LBV stars (50–600 km s^{-1}) is shown in blue (Smith 2014) and the expected wind speed range of RSG stars (10–50 km s^{-1}) shown in red (van Loon 2005)) is shown as the red shaded region. The data for each He line are offset by +0.05 d in phase for clarity. Errors are largely dominated by the resolution of the instruments.

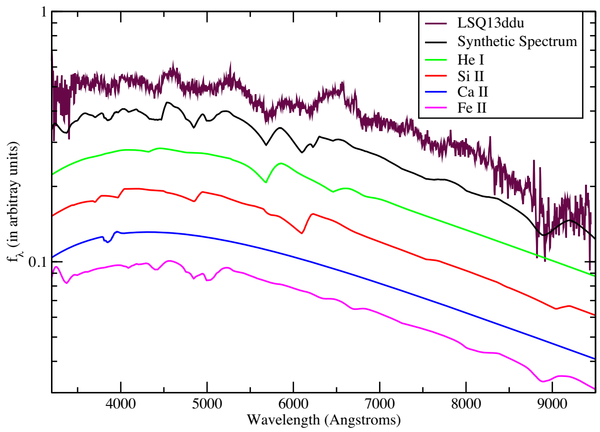

Figure 12. The +9 d spectrum of LSQ13ddu (purple) along with the best SYNAPPS fit (black). The individual line identifications for the unambiguously determined ionic species of He I (green), S II (red), Ca II (blue), and Fe II (magenta) are plotted underneath. All have a photospheric velocity of 10 200 km s^{-1}. Additional, weaker lines from O I, Co II may also be present, but do not significantly contribute to the spectral fit.

light curve contains one SN Ib (SN 2007Y), two broad-lined Ic SNe (Ic-BL, SNe 2002ap and 2007D) with the remaining six objects classified as SNe Ic. This template light curve was then subtracted from the LSQ13ddu light curve to obtain the additional luminosity component required to power the light curve. We find at least qualitatively using this comparison that the light curve of LSQ13ddu could be powered by an underlying SE-SN with a contribution at early times from CSM interaction (right-hand panel of Fig. 13). This is supported by the weakening of the narrow CSM linked He I features which are not detected in the spectra of LSQ13ddu at phases greater than +11 d post maximum. The late-time spectra much more closely resembling those of a SE-SN. We also explored the plausibility of a light curve with a CSM contribution through photometric modelling of LSQ13ddu (see Section 3.5).

3.5 Photometric modelling

A number of photometric modelling codes using semi-analytic models to provide fits to the observed light curves of SNe and other transients have become available in recent years, such as MOSFIT (Guillochon et al. 2018) and TIGERFIT (Chatzopoulos 2018). In this section, we discuss the use of MOSFIT[6] to produce model fits to the light curve of LSQ13ddu. We chose to use MOSFIT due to its configurable nature, both in terms of the model to apply and the parameter inputs which can be constrained based on available observational data. Additionally, MOSFIT is a Monte Carlo code and as such provides more robust statistical uncertainties on its output results than some other codes.

MOSFIT has previously been used to model the photometric properties of SLSNe (Nicholl, Guillochon & Berger 2017) and in the wider exploration of the duration-luminosity phase space occupied by astrophysical transients (Villar et al. 2017). One of the main limitations of MOSFIT is the assumption of single (or multiple) blackbodies to describe the SED, which is not appropriate for objects whose spectra deviate significantly from a blackbody due to the presence of strong absorption or emission features.

---

[6] MOSFIT version 1.1.1 was used throughout this work.

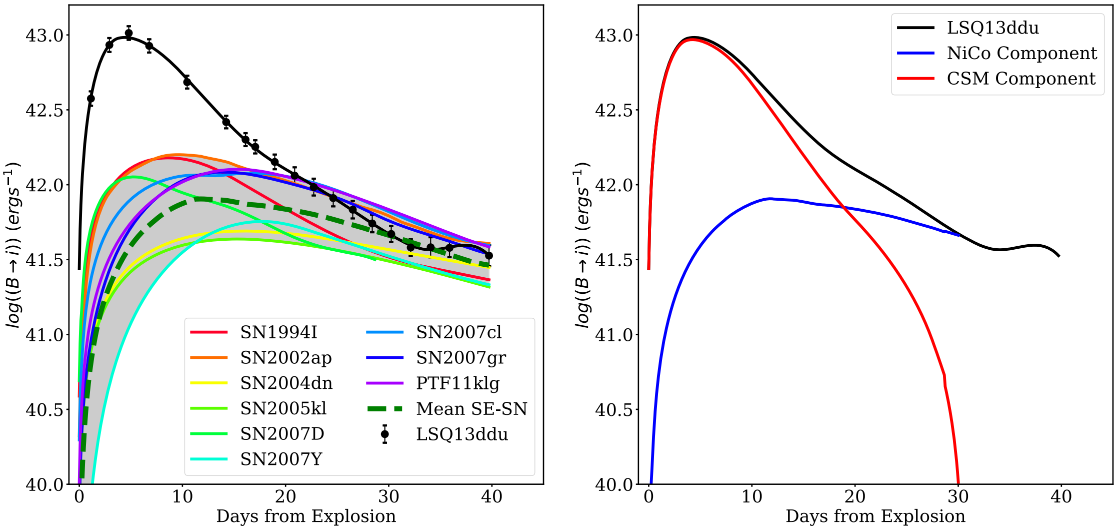

Figure 13. Left-hand panel: The bolometric light curve (black data points with black solid line) of LSQ13ddu compared to a subset of SE-SNe from (Prentice et al. 2016) showing similar late-time photometric behaviour. The individual events are shown as coloured solid lines and the grey shaded region highlights the range within this sample. A SE-SN template was calculated as the mean value of this range, shown as a green dashed line. Right-hand panel: A comparison showing the additional flux required above that provided by the mean SE-SN template assuming SE-SNe are powered by radioactive ^{56}Ni decay (NiCo component, blue solid line). The additional flux needed to power the light curve of LSQ13ddu (shown in black) is shown to arise from CSM interaction (shown as a red solid line).

For LSQ13ddu, an assumption of a blackbody SED is appropriate around maximum light but less so at later times when its spectra are dominated by broad emission and absorption features. MOSFIT has also not been previously applied to such a rapidly evolving transient that is modelled with both CSM and nickel-powered components. As such, the results of these semi-analytic models should be treated as indicative of the applicability of a powering mechanism rather than quantitative constraints on the specific configuration of the CSM or the ejecta mass required. For further limitations of modelling with MOSFIT see Nicholl et al. (2017) and Villar et al. (2017).

Based on our earlier analysis of the photometric and spectroscopic evolution of LSQ13ddu, we compared the light curves of LSQ13ddu to three potential powering models: (i) radioactive ^{56}Ni decay, (ii) CSM-interaction driven, and (iii) magnetar spin-down. MOSFIT has a combined ^{56}Ni + CSM model that has been used to model high mass, superluminous SNe (SLSNe Nicholl et al. 2017). The CSM aspect of this model is based on the work of Chatzopoulos et al. (2013), and makes several assumptions that, while appropriate for use in modelling high-mass SLSNe, limit its applicability to fast-evolving events with low CSM masses. In particular, the diffusion time within the model is significantly overestimated and as such when presented with a fast-evolving light curve, the model favours a very low CSM and ejecta mass with an increased ejecta velocity. This leads to the model drifting to a region where other underlying assumptions (e.g. the diffusion of the products of ^{56}Ni decay through both the ejecta and optically thick region of the CSM) become less applicable. As such we do not employ this model in this analysis.

Instead to measure a potential CSM contribution to the light curve with MOSFIT, we fitted the two components obtained in Section 3.4 separately, with this choice ensuring the CSM assumptions (and their associated uncertainties) only affect the CSM contribution and not the standard ^{56}Ni model. The ejecta velocity of the CSM component was allowed to reach values much higher than was observed to compensate for the overestimated diffusion time discussed above.

As inputs, MOSFIT took a number of parameters constrained from the photometric and spectroscopic observations of LSQ13ddu, such as the inferred explosion date, minimum blackbody temperature, and host galaxy extinction. Where no strict constraints were available, broad priors were placed on these parameters. Following previous work, we assumed that the optical opacity, κ, is in the range 0.05–0.1 cm^2 g^{-1} and the gamma-ray opacity, κ_γ, is in the range 0.01–0.1 cm^2 g^{-1} (e.g. Swartz, Sutherland & Harkness 1995; Wheeler, Johnson & Clocchiatti 2015; Wang et al. 2017). The photosphere for the models makes use of a temperature floor with a single value taken from an allowed range of 4000–7000 K, which is constrained based on the derived temperature measurements (see Section 3.2). The variables and their input values or ranges used for each of the models are described in Table 5. The fits were made using a Markov chain Monte Carlo routine implemented in MOSFIT utilizing the EMCEE python package (Foreman-Mackey et al. 2013). A description of the main features of the three input models is provided below.

3.5.1 *Radioactive ^{56}Ni decay*

The bulk of SE-SN light curves can be explained by the radioactive decay of ^{56}Ni (e.g Woosley et al. 1994). Due to the high peak luminosity and rapid rise of LSQ13ddu, we used MOSFIT to explore if a physically realistic configuration of ^{56}Ni decay based on the model of Nadyozhin (1994) could generate the observed light curve. The ^{56}Ni mass fraction has been constrained to be <0.6 of the ejecta mass, which includes the range expected of CC-SNe (~0.2; Umeda & Nomoto 2008) extending to the higher values observed in SNe Ia. This model is fitted to the photometric data available from explosion to 29 d past maximum. The exclusion of the data at later phases is to reduce the effect of a non-constant opacity at later times on the validity of the underlying model assumptions. We also fit the underlying ^{56}Ni component determined through the photometric analysis outlined in Section 3.4 to test if this component is consistent with that of a ^{56}Ni decay-powered event.

Table 5. Input parameters and their allowed ranges for the MOSFIT models explored in this work: a ^{56}Ni only model fit to the optical pseudo-bolometric light curve, a ^{56}Ni model fit to the underlying SE-SN light curve 'SE-SN component', a 'CSM Component' for the corresponding CSM interaction contribution, and the magnetar model.

Parameter	Input range	Output value
^{56}**Nionly model:**		
Ejecta mass ($M_\odot$)	0.01–10	$0.07^{+0.05}_{-0.03}$
Ejecta velocity ($\mathrm{km\,s^{-1}}$)	9000–11 000[a]	$10\,000^{+700}_{-700}$
^{56}Ni fraction	0.001–0.6	$0.13^{+0.25}_{-0.12}$
^{56}Ni mass ($M_\odot$)	10^{-5}– 6	$0.01^{+0.04}_{-0.01}$
SE-SN component:		
Ejecta mass ($M_\odot$)	0.01–10	$1.30^{+0.43}_{-0.34}$
Ejecta velocity ($\mathrm{km\,s^{-1}}$)	9000–11 000[a]	$10\,100^{+600}_{-700}$
^{56}Ni fraction	0.001–0.6	$0.06^{+0.02}_{-0.01}$
^{56}Ni mass ($M_\odot$)	10^{-5}– 6	$0.08^{+0.06}_{-0.03}$
CSM component:[b]		
Ejecta mass ($M_\odot$)	0.01–10	$0.08^{+0.07}_{-0.04}$
CSM mass ($M_\odot$)	0.01–10	$0.59^{+0.19}_{-0.14}$
$\log_{10}$ (CSM density) ($\mathrm{g\,cm^{-3}}$)	$-16 - -10$	$-10.99^{+0.58}_{-0.69}$
Progenitor radius (au)	0.01–5	$1.58^{+1.94}_{-0.80}$
Ejecta velocity ($\mathrm{km\,s^{-1}}$)	9000–50 000[c]	$34\,600^{+8,200}_{-7,100}$
Magnetar:		
Ejecta mass ($M_\odot$)	0.01–10	$0.02^{+0.02}_{-0.00}$
Ejecta velocity ($\mathrm{km\,s^{-1}}$)	9000–11 000[a]	$10\,100^{+700}_{-800}$
Spin period (ms)	1–10	$7.34^{+1.89}_{-2.70}$
B Field (10^{14} G)	0.1–10	$0.30^{+0.93}_{-0.16}$

[a] From SYNAPPS fitting and He I 10 830 Å line measurements.
[b] For an isotropic, wind-like CSM with a density profile $s = 2$.
[c] Expanded range to compensate for the model's diffusion time overestimation.

3.5.2 *CSM-powered light-curve contribution*

To determine if the CSM component identified by the light-curve analysis in Section 3.4 is compatible with physically realistic parameter values, we have fit it with the MOSFIT CSM interaction model. As discussed above, this CSM model is based on Chatzopoulos et al. (2013) and is subject to the same limitations.

In Chatzopoulos et al. (2013), a parameter study was conducted to explore the robustness of the parameter outputs of the CSM model on which MOSFIT is based. Specifically, they tested changing the CSM density profile from that of a shell ($s = 0$) to being wind-like ($s = 2$) and found that there is a factor of 2–3 uncertainty in the majority of the parameters, with the exception of the ejecta mass and progenitor radius which differed by up to an order of magnitude, despite not producing significantly different light curves.

The CSM configuration of LSQ13ddu and other such events is uncertain, both because there is still debate as to their progenitor systems which likely plays a significant role, and the difficulty in determining the configuration from available observations. We have chosen to model the CSM with a wind-like profile but the true configuration is unknown.

3.5.3 ^{56}*Ni decay and CSM modelling results*

We found that the rapid rise and bright peak luminosity of LSQ13ddu cannot be fit with the purely ^{56}Ni-powered model. The output parameters for this fully ^{56}Ni-powered model are given in Table 5 and shown in the left-hand panel of Fig. 14. Therefore, we explored if the light curve could be explained by a combination of a ^{56}Ni and a CSM component by fitting each component separately. We found that MOSFIT was able to produce a good fit to the underlying ^{56}Ni component with a ^{56}Ni mass of ∼0.08 $M_\odot$ and an ejecta mass of ∼1.30 $M_\odot$. The early flux excess in LSQ13ddu as seen in Fig. 13 was found to be well fit by the MOSFIT CSM interaction model with a CSM mass of ∼0.6 $M_\odot$, a density of $\sim 1\mathrm{x}10^{-11}\ \mathrm{g\,cm^{-3}}$, and initial/progenitor radius of ∼1.6 au. As noted above, by Chatzopoulos et al. (2013) the ejecta mass and progenitor radius are the most weakly constrained parameters and may have systematic uncertainties of up to an order of magnitude depending on the CSM input parameters.

The output parameters are outlined in Table 5 with the two component fits shown in the right-hand panel of Fig. 14. Several parameters are shared between the ^{56}Ni and CSM models (opacity, minimum temperature floor, explosion epoch, host extinction contribution, ejecta mass and ejecta velocity) with good agreement between the majority. However, there is significant tension between the values of two parameters: ejecta velocity and ejecta mass. The tension in the fitted values of ejecta velocity was previously described as a consequence of the overestimated diffusion time of the CSM model for fast evolving events like LSQ13ddu. The tension in the values of ejecta mass ($1.30^{+0.43}_{-0.34}$ $M_\odot$ for the ^{56}Ni component and $0.08^{+0.07}_{-0.04}$ $M_\odot$ for the CSM component) is most likely due to the propagation of the CSM density profile uncertainties (Chatzopoulos et al. 2013), as well as the manner in which the model treats diffusion time-scales and the resulting increased ejecta velocity. Despite these caveats, the results of this modelling show that the use of two distinct power sources (combined ^{56}Ni and CSM) fits the light curve of LSQ13ddu well.

3.5.4 *Photometric modelling of magnetar powering*

For some luminous and rapidly evolving transients such as iPTF16asu (Whitesides et al. 2017) and AT 2018cow (Prentice et al. 2018b), powering through the spin-down of a magnetar has been investigated. Since LSQ13ddu also displays a fast rise and high peak luminosity, we have tested if LSQ13ddu could be fit by a magnetar model. We find that the best-fitting models, while able to reproduce the shape of the light curve, have several output parameters that appear physically unlikely. For models both with and without a constraint on the expansion velocity to match the observed velocities of 9000–11 000 $\mathrm{km\,s^{-1}}$, the ejecta mass is extremely low (∼0.02–0.04$M_\odot$). When the model velocities are constrained to realistic values, it is also unable to replicate the observed light-curve shape, with the peak luminosity underestimated as shown in Fig. 15. Very low ejecta masses have previously been seen in purely magnetar fits to iPTF16asu (Whitesides et al. 2017) and a range of fast transients in Arcavi et al. (2016) with these being disfavoured as powering sources as the massive star progenitors for such objects would require excessive envelope stripping to produce explosions

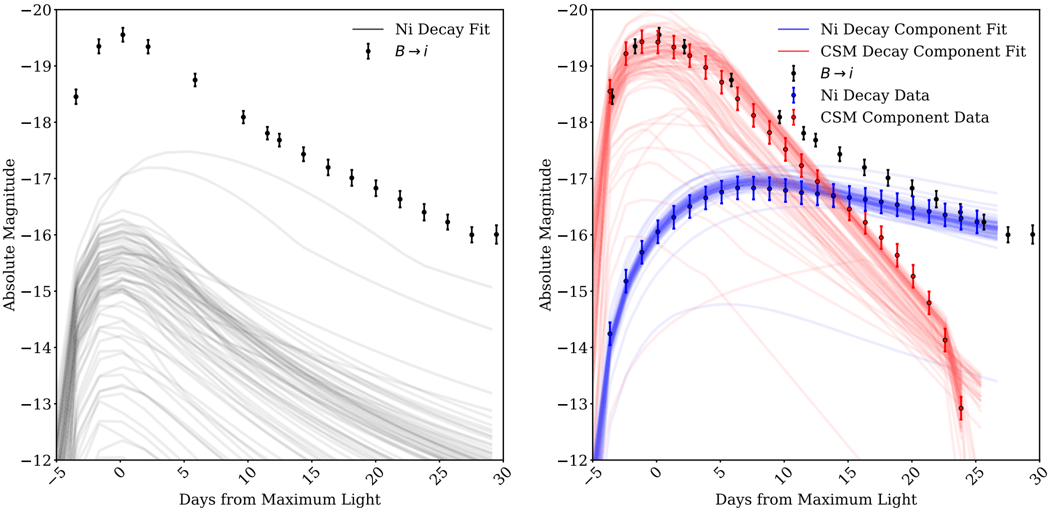

Figure 14. Left-hand panel: Comparison of the light curves produced using MOSFiT for a ^{56}Ni powered light curve with a limit on the ^{56}Ni to total ejecta mass fraction of <0.6. The optical bolometric light curve points are in black and the fitted light curves with the top 25 percent of scores are shown in grey. Right-hand panel: The ^{56}Ni model outputs compared to the SE-SN light-curve component identified in Section 3.4. The optical bolometric light curve points are in black and the fitted light curves with the top 25 percent of scores of the ^{56}Ni fit are shown in blue with the corresponding fitting of the CSM component shown in red.

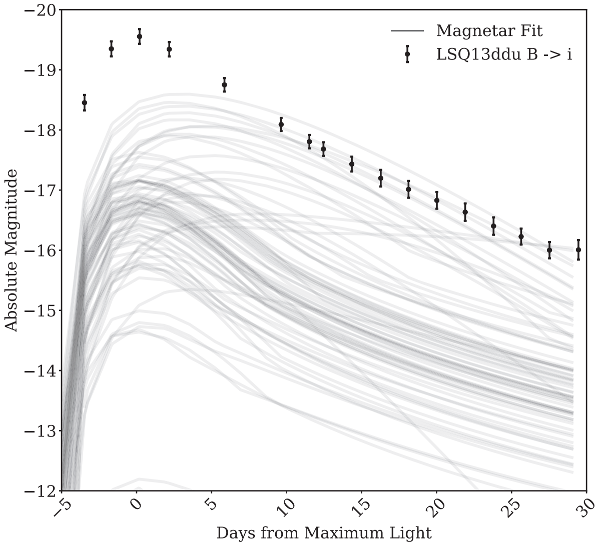

Figure 15. Comparison of the light curves produced using MOSFIT for a magnetar-powered light curve with parameters outlined in Table 5. The optical bolometric light curve points are in black and the fitted light curves with the top 25 percent of scores are shown in grey.

with such low ejecta masses. We disfavour the magnetar spindown model for LSQ13ddu for the same reason.

4 DISCUSSION

New classes of rapidly evolving transients have been discovered in recent years and attempts have been made to divide these into sub-classes arising from distinct progenitor pathways. LSQ13ddu is one such rapidly evolving transient that challenges existing progenitor scenarios. It displayed a rapid photometric evolution, early spectroscopic features similar to, but significantly weaker than those seen in SNe Ibn, before developing broad spectral features more similar to SE-SNe. In this section, we compare the photometric and spectroscopic properties of LSQ13ddu with those of both common and rare transient sub-classes to attempt to place it in the context of previous events. We also discuss the evidence for this being a hybrid SN Ibn and the implications this has for its progenitor scenario.

4.1 Light-curve comparisons

In Fig. 16, we compare the *LSQgr* light curve of LSQ13ddu with those of a sample of fast-evolving SE-SNe and unusual transient events (see Table 6 for details of the comparison objects). Each light curve has been fitted using a smoothed cubic spline with their observed time of maximum light taken from the source work where possible or otherwise obtained from the spline fit. Each light curve has also been scaled to match the peak of LSQ13ddu to better study any differences in relative evolution.

Overall, as in the comparison of the (optical) pseudo-bolometric light curves, the scaled light-curve behaviour of LSQ13ddu is most similar to that of the Ibn SN 2014av (Pastorello et al. 2016), with both showing a nearly identical rise time and initial decay rate (0.15 ± 0.01 and 0.13 ± 0.01 mag d^{-1}, respectively, during the first 15 d post maximum). The decline rate of LSQ13ddu slows to 0.09 ± 0.02 mag d^{-1} between 20 and 35 d after maximum, which is similar to that of the Ic-BL SN 2007ru, which declines at a rate of 0.09 ± 0.01 mag d^{-1} at a similar phase.

In contrast, the behaviours of SNe 2010X (Kasliwal et al. 2010) and 2002bj (Poznanski et al. 2009) differ significantly from LSQ13ddu, with both showing slower initial relative decline rates that increase over time so that their overall decline is more rapid than that of LSQ13ddu. These events are significantly less luminous with peak absolute magnitudes of −16.6 and −18.8 mag for SNe 2010X and 2002bj, respectively, compared to the −19.6 mag of LSQ13ddu. The origin of these events remains unclear but they could be He-shell detonations on the surface of a white dwarf ('.Ia SN') or ultra-stripped SNe (USSNe).

USSNe are a proposed class linked to rapidly fading transients that are thought to be produced through the interaction of evolved

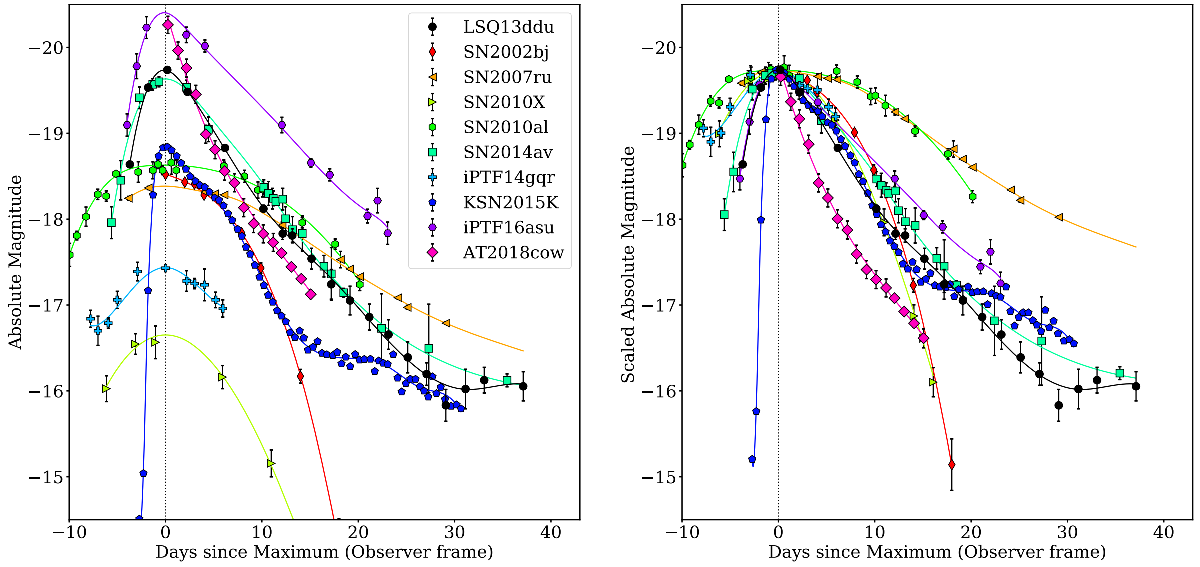

Figure 16. Left-hand panel: Absolute magnitude *R*-band light curves of a sample of literature objects compared to the *LSQgr*-band light curve of LSQ13ddu. Right-hand panel: The light curves of the comparison objects have been scaled to match the peak of LSQ13ddu. The solid lines in both panels display the smoothed cubic spline fit to the observations. Details of the comparison objects are given in Table 6.

Table 6. Summary of the comparison objects used in Fig. 16, showing the object name, its predicted type, the peak *R*-band magnitude, R_{max}, and Δm_{15}.

Object	Classification	R_{max} (mag)	Δm_{15} (mag)	Ref.
LSQ13ddu	–	– 19.7[a]	2.2	–
SN 2002bj	.Ia or SE-SN[b]	– 18.5	2.8	1
SN 2007ru	Ic-BL	– 18.4	0.7	2
SN 2010X	.Ia or USSN[b]	– 16.7	2.7	3
SN 2010al	hybrid Ibn	– 18.6	0.7	4
SN 2014av	Ibn	– 19.6	2.0	5
iPTF14gqr	USSN[b]	– 17.4	0.5	6
KSN2015K	SB[b]	– 18.8	2.3	7
iPTF16asu	Magnetar and/or SB[b]	– 20.4[c]	1.7	8
AT 2018cow	?	– 20.2	3.2	9

Notes.
[a] LSQ13ddu value is given using *LSQgr*-band data.
[b] USSN = Ultra-stripped SN. SB = shock-breakout into CSM. SE-SN = Stripped envelope SN.
[c] iPTF16asu value is given using *g*-band data. References: (1) Poznanski et al. (2009), (2) Sahu et al. (2009), (3) Kasliwal et al. (2010), (4) Pastorello et al. (2015a), (5) Pastorello et al. (2016), (6) De et al. (2018), (7) Rest et al. (2018), (8) Whitesides et al. (2017), (9) Prentice et al. (2018b)

massive stars, which have lost the majority of their envelopes via stripping by a neutron star in a close binary orbit (Tauris, Langer & Podsiadlowski 2015). iPTF14gqr (De et al. 2018), and perhaps SN 2010X (Moriya et al. 2017), have been suggested to be members of this class. USSNe reach a *V*-band peak of approximately −16 mag, while LSQ13ddu is brighter by more than a factor of 100 at a peak of −19.7 mag. This drastic difference in peak luminosity leads us to rule this class out as a physical explanation for LSQ13ddu.

In Fig. 17, the optical bolometric light-curve peak magnitude, the rise time, and the decline rate over the first 15 d post peak (Δm_{15}) are compared to a sample of SE-SN full bolometric light curves from Lyman et al. (2016), supplemented with SN Ibn data from Hosseinzadeh et al. (2017) and 'fast' transients from Drout et al. (2014). The magnitudes quoted for the Ibn sample are not bolometric but are *R*-, *r*-, or *g*-band values, with the objects from Drout et al. (2014) given in *PS1-r* (Tonry et al. 2012). The offset between the *R* and the optical bolometric magnitude for LSQ13ddu is 0.84 mag, while the offset between the optical and full bolometric magnitude of LSQ13ddu is much smaller at 0.24 mag, with a similar 0.16 mag value determined for the *g* band, suggesting that the use of the *R*/*r* or *g*-band magnitudes for the Ibn sample is valid.

The light-curve properties of LSQ13ddu are located with the parameter space occupied by the SNe Ibn class, with brighter peak magnitudes and a faster photometric evolution (rise and decay) that those of 'normal' SE-SNe. In comparison to the 'fast' transients of Drout et al. (2014), LSQ13ddu has a slower rise and larger Δm_{15} value than the bulk of the sample, which can reach their peak luminosity in as little as day and decay more slowly after peak. While the available spectra of these objects are limited, those that are available do not provide good matches to those of LSQ13ddu and we conclude that they are more likely to represent a distinct class of objects.

4.2 He velocities and the connection to pre-explosion mass-loss

Fig. 18 shows the absorption minimum velocities of the He I lines in LSQ13ddu, compared to a sample of SNe Ibn with velocity measurements within 20 d of maximum light obtained from Pastorello et al. (2016). As discussed in Section 3.3.2, the He I velocity of LSQ13ddu of 250 ± 20 km s^{-1} is the weighted mean of the measurements in the two highest resolution spectra. As can be seen in Fig. 18, this value is lower than the majority of SNe Ibn. The three objects with the most similar He I velocities to those of LSQ13ddu are PS1-12sk (Sanders et al. 2013), SN 2011hw (Smith et al. 2012; Pastorello et al. 2015a), and SN 2005la (Pastorello et al. 2008b) with velocities of 130, 200–250, and 500 km s^{-1}, respectively (Pastorello et al. 2016). These objects, along with LSQ13ddu, fall in the range of wind velocities normally seen for LBV and outside the range typically seen for WR stars of 500–3200 km s^{-1} (Crowther 2007).

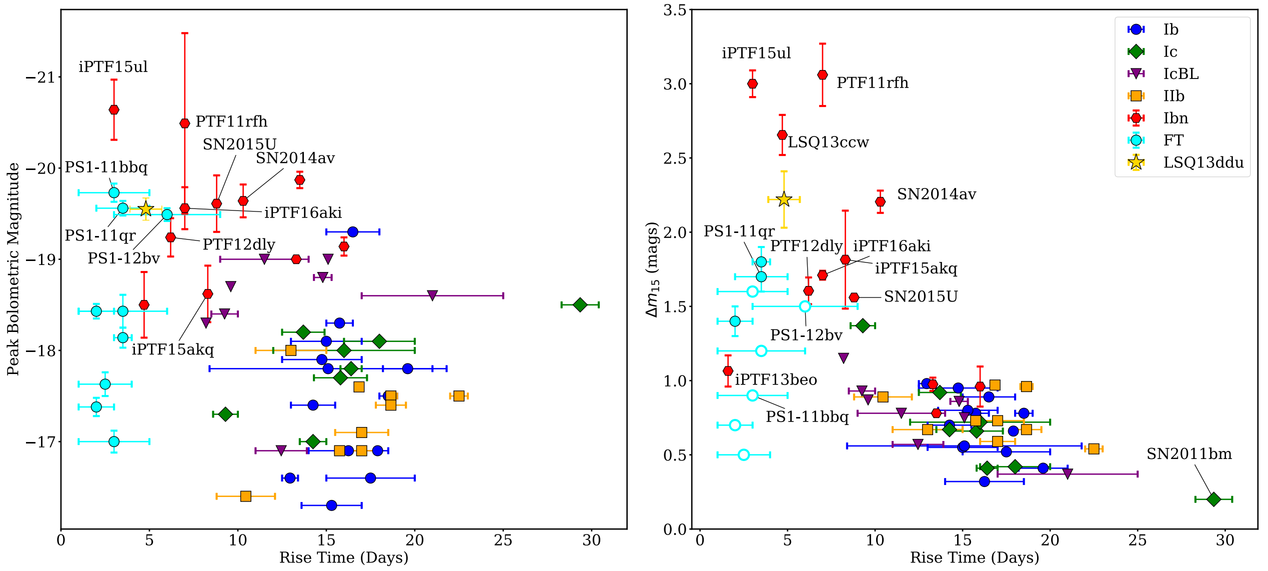

Figure 17. Left-hand panel: Peak bolometric magnitudes of a sample of SE-SNe from Lyman et al. (2016) are plotted against their bolometric rise times to peak. For the Ibn sample of Hosseinzadeh et al. (2017) the values shown are those of the *R*-, *r*-, or *g*-band data, with the 'fast' transients from Drout et al. (2014) shown using *PS1-r* data. Right-hand panel: The decline rates in the first 15 d post-maximum light are shown against their bolometric rise times. The open markers indicate where the Δm_{15} value is a lower limit. The different classes of objects are colour-coded as detailed in the legend, with LSQ13ddu shown as a yellow star.

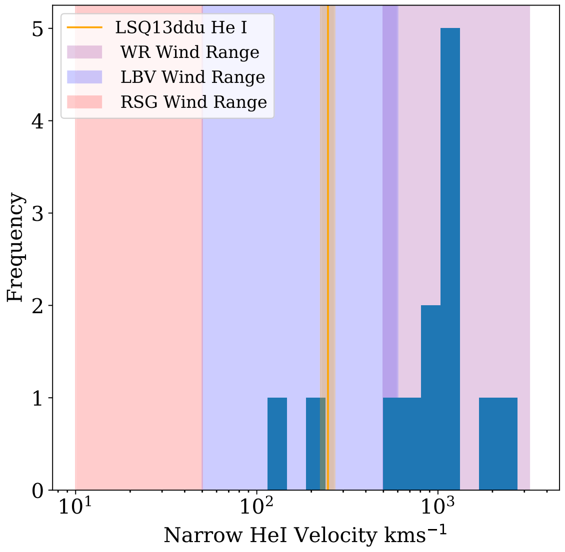

Figure 18. The mean narrow He I velocity of LSQ13ddu as a weighted mean of the He I features visible in the +5 and +6 d spectra (250 ± 20 km s^{-1}, shown in yellow with its uncertainty shown by shading), compared to a literature sample of SNe Ibn obtained from Pastorello et al. (2016) (blue histogram). The wind speed ranges for WR, LBV, and RSG stars are indicated by the purple, blue, and red shaded regions, respectively. The three SNe Ibn in the LBV wind range other than LSQ13ddu are PS1-12sk, SNe 2011he, and 2005la in order of increasing velocity.

Red supergiants have winds that are much slower, with values of a few tens of km s^{-1} (van Loon 2005).

As discussed in Section 3.3.2, without the availability of higher resolution (∼35 km s^{-1}) spectra for LSQ13ddu, we would have measured a significantly higher He I velocity of up to ∼850 km s^{-1} that would be more in agreement with the majority of SNe Ibn.

To determine the role that spectral resolution plays in the obtained velocities for narrow features in SNe Ibn, we investigated the SN Ibn sample of Pastorello et al. (2016). We found that the SNe Ibn with the lowest velocities, such as PS1-12sk and SN2011hw, have spectra with higher than normal resolution suggesting that there may be other objects that have similarly low He I velocities (<500 km s^{-1}) but did not have spectral measurements at high enough resolution. However, there are a number of SNe Ibn with high He I velocities (>1000 km s^{-1}) that have sufficiently high spectral resolution where lower velocities could have been resolved e.g. SN 2010al. Therefore, we conclude that there is an intrinsically wide range in He I velocities in SNe Ibn but that the percentage with low He I velocities may be underestimated due to the resolution of the spectra.

SNe Ibn have been associated with explosions of WR stars because of the similar velocities of their winds and the He I features in SNe Ibn, as well as the H-free nature of WR atmospheres that matches with the H-free spectra of SNe Ibn (Pastorello et al. 2008a). The objects that have He I velocities most similar to LSQ13ddu and fall in the LBV wind range all displayed some degree of peculiarity. PS1-12sk was found in an old stellar population and was suggested to be associated with a white dwarf transient or a rare massive star event in a low star-formation region (Sanders et al. 2013; Hosseinzadeh et al. 2019). SN 2011hw and SN 2005la both displayed narrow H α lines in their spectra suggesting they are transitional between Type Ibn and Type IIn events (Pastorello et al. 2008b) and perhaps consistent with stars exploding during the LBV to WR transition (Pastorello et al. 2016). As discussed in Section 3.3.1, based on the line widths, the SN-related contribution to the H α flux is consistent with zero, though a minority contribution cannot be ruled out. This is at odds with the H-rich composition expected in LBVs. Therefore, it appears difficult to match LSQ13ddu to a particular progenitor scenario given its combination of observed properties, but we discuss potential systems in Section 4.5.

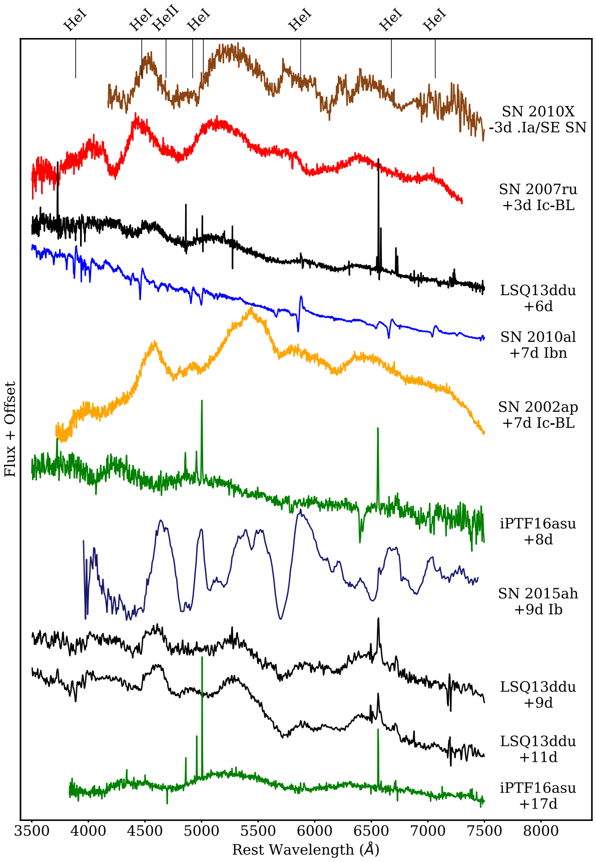

Figure 19. Spectral comparison between LSQ13ddu (black), the Ic-BL SNe 2007ru (red) (Sahu et al. 2009), and 2002ap (orange) (Modjaz et al. 2014), the Type Ib SN 2015ah (light blue) (Prentice et al. 2019), the Ibn SN 2010al (dark blue) (Pastorello et al. 2015a) iPTF16asu (green) (Whitesides et al. 2017), and the unusual SN 2010X (brown) (Kasliwal et al. 2010). The vertical ticks mark the location of the He lines.

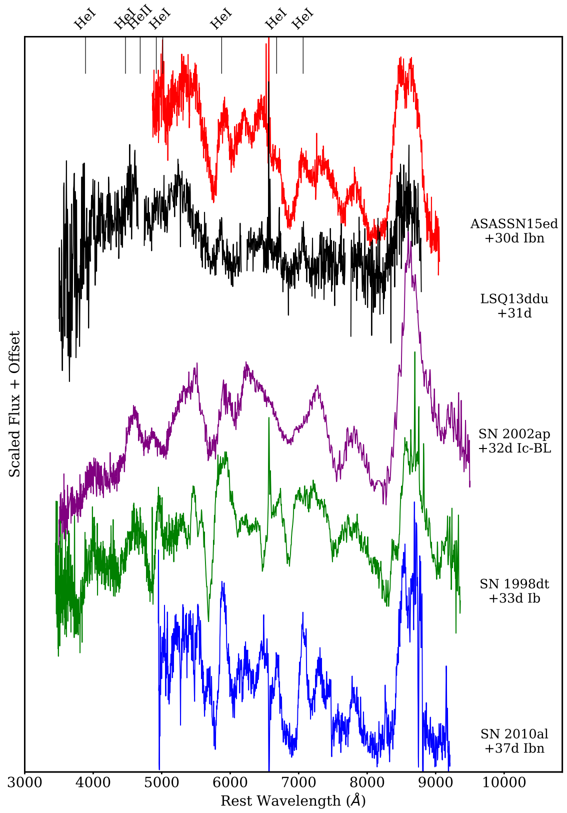

Figure 20. A spectral comparison of the broad spectral features in LSQ13ddu with a sample of SE-SNe and Ibn to Ib hybrid event. The vertical lines mark the location of the He lines for clarity.

4.3 Is LSQ13ddu a hybrid SNe Ibn?

Some SNe Ibn, such as SN 2010al (Pastorello et al. 2015a) and ASASSN-15ed (Pastorello et al. 2015d), show hybrid properties between those of 'normal' Ibn and Ib SNe, with narrow He I CSM features in their early spectra along with broad He features coming from He-rich ejecta at late times. LSQ13ddu displays a number of spectral similarities to SN 2010al, with both displaying narrow WR wind-related features in their earliest spectra. SN 2010al displayed early-time spectral features indicative of material related to CNO-cycle enrichment in the wind of the progenitor star but these are not seen in LSQ13ddu. Transitional Ibn to Ib SNe show a broad diversity in their light curves and do not form a separate subclass based on their light curves alone.

A spectral comparison between the +6–11 d spectra of LSQ13ddu with a sample of SE-SNe and Ibn events (including the hybrid Ibn to Ib SN 2010al) is shown in Fig. 19. The broad spectral features in LSQ13ddu most closely resemble those of SNe Ic-BL, such as SN 2007ru (Sahu et al. 2009) and SN 2002ap (Modjaz et al. 2016), particularly in the 4450–4750, 5250–5800 and 6250–6700 Å regions, though the continuum of the latter is redder than that of LSQ13ddu. As discussed in Section 3.3.2, SN 2010al displays strong narrow He I features that are not seen in LSQ13ddu at the same epoch, suggesting a faster evolution for LSQ13ddu. SYNAPPS fitting (Fig. 12) showed that the broad optical features seen at +9 d in LSQ13ddu can be explained by lines of Fe II, Ca II, O I, C III, along with He I features at the same photospheric velocity (10 200 km s^{-1}). A broad He I 10 830 Å feature is seen in the +9 and +14 d of LSQ13ddu with a FWHM velocity of ~9500 km s^{-1}, suggesting underlying ejecta with He present.

The late-time (+31 d) spectrum of LSQ13ddu is compared in Fig. 20 to those of the transitional Ibn to Ib events, SN 2010al and ASASSN-15ed, as well as Ib SN 1998dt and the Ic-BL SN 2002ap (Modjaz et al. 2014). The spectrum of LSQ13ddu is most similar to the transitional Ibn to Ib SNe that display broad He I features (FWHM of 5000–6000 km s^{-1}) but it has significantly weaker He I features. This suggests that LSQ13ddu may be a transitional Ibn to Ic SN with a small amount of residual He present within the ejecta. Such residual He has previously been seen in other SNe Ic e.g. the Ic-BL SN 2016coi, which displayed traces of He I within its ejecta (Prentice et al. 2018a).

The light curve of LSQ13ddu is well fit with the early peak brightness being powered by CSM interaction before an underlying ^{56}Ni decay component becomes dominant at ~10 d post peak brightness. Hybrid Ibn such as SN 2010al and ASASSN-15ed are suggested to be powered at early times by CSM interaction and although they have stronger He I interaction features at early times compared to LSQ13ddu, the differences in line strength may represent a continuum of CSM properties (e.g. mass and density profiles). The next weakest He I features were those of ASASSN-15ed, which was also a hybrid Ibn to Ib event. A full understanding of the connection between the strength of the narrow He features and properties of the underlying CSM is difficult and would require detailed knowledge of the CSM, as well as consideration of non-thermal effects (Boyle et al. 2017).

No intermediate and broad components due to shocked CSM are seen in LSQ13ddu, which is also the case in ~50 percent of Ibn SNe (Hosseinzadeh et al. 2017). The preferred scenario to explain the lack of intermediate-width features is the presence of an optically thick outer CSM reprocessing the shocked material that masks these intermediate-width features (Chevalier & Irwin 2011; Ginzburg & Balberg 2012; Pastorello et al. 2015c; Hosseinzadeh et al. 2017).The geometric configuration of the system along with effects of viewing angles can also mask the appearance of ejecta–CSM interaction signatures from the observed spectra of some objects e.g. iPTF14hls (Andrews & Smith 2018). In this case, it has been proposed that fast SN ejecta may obscure CSM ongoing ejecta – CSM interaction that is predominately occurring in an equatorial disc. Given the previously described uncertainty in the CSM configuration, along with supporting observational and theoretical studies, the absence of intermediate width lines does not exclude a significant contribution from CSM interaction to the luminosity of LSQ13ddu.

4.4 Search for a GRB companion

A subset of Ic-BL SNe has been found to have accompanying long-duration gamma ray bursts (GRBs) (Woosley, Eastman & Schmidt 1999; Woosley & Bloom 2006). Since the later time spectra of LSQ13ddu have some similar broad features to those of Ic-BL SNe, we conducted a search in the Fermi GBM Burst Catalogue (Paciesas et al. 2012; Gruber et al. 2014; Bhat et al. 2016) for events coincident with LSQ13ddu. Specifically, we searched for triggers within 15 deg of the spatial location of LSQ13ddu within the time period covering one week prior to its first optical detection. One such event was identified meeting these criteria – GRB131123A. GRB131123A was detected on 2013 November 23.5 (MJD 56619.5), which is 2.8 d prior to the first optical detection of LSQ13ddu and 0.8 d before the last *LSQgr* non-detection at a limiting magnitude of >21.84 mag. Samples of Ic-BL SNe with associated GRBs do not show significant lag times between the GRB and the optical transient (e.g. Woosley & Bloom 2006; Cano et al. 2017). GRB131123A occurred at RA 53.240 deg, Dec. −20.880 deg (J2000) with a statistical uncertainty on the position of 8.34 deg (Fermi GRB Team 2013). The location of LSQ13ddu is outside this error region at a separation of 10.7 deg from the GRB position. Furthermore, its T_{90} duration was 3.14 ± 0.72 s, placing it in the intermediate region between short and long GRBs (Paciesas et al. 1999). Given the offset in the locations, the delay between the GRB and the first visible detection of the SN, and the relatively short GRB duration compared to typical Ic-BL-GRB SNe, we conclude that GRB131123A is an unrelated event.

4.5 The potential progenitor system of LSQ13ddu

The progenitors of SNe Ibn have been proposed as evolved WR stars that explode before the residual CSM from prior mass-loss events (either winds or outbursts) have dissipated. This poses a problem for stellar evolution models as WR stars are expected to survive for a sufficient period of time prior to a SN explosion for such material to have dissipated (e.g. Meynet & Maeder 2005). Alternatively, interacting binary systems have also been proposed as possible progenitors for SNe Ibn (Pastorello et al. 2008a). The prototype for the Ibn class, SN 2006jc, was observed to undergo a large eruptive mass-loss event approximately two years prior to its terminal explosion (Pastorello et al. 2007). Such events are problematic for single-star progenitor scenarios as no WR star has yet been observed to undergo significant mass-loss events. This may be alleviated if the SN 2006jc system consisted of an LBV and a WR star, with the LBV responsible for the outburst before its companion WR exploded in the years following this explosive mass-loss episode. This scenario, however, is somewhat fine-tuned and is unlikely to explain the full class of Ibn objects.

If SNe Ibn are produced though the explosion of WR stars or stars in a transition phase from LBV to WR, the velocity of the CSM should be consistent with measurements of these classes of objects. The bulk of observed SNe Ibn have CSM expansion velocities consistent with those of WR stars. However, a subset of Ibn, as well as LSQ13ddu, have lower wind velocities ($250 \pm 20\ \mathrm{km\,s^{-1}}$), more consistent with those of LBV stars (see Fig. 18). The narrow He I features of LSQ13ddu are also weaker compared to the general SNe Ibn population at similar phases. Due to a lack of higher resolution spectra for some SNe Ibn, we have found that a larger percentage of SNe Ibn than previously thought may have lower He I velocities that are more consistent with LBV, instead of WR-like winds, although as previously discussed, the composition of these winds does not match what is expected of a H-rich LBV star.

Similar to the hybrid Ibn/Ib SNe 2010al and ASASSN-15ed, LSQ13ddu evolves from an early blue continuum to show broad features consistent with He-containing ejecta. The amount of He present in the ejecta (not the CSM component) appears to be lower in LSQ13ddu compared to both Ib SNe and these hybrid events, with LSQ13ddu having weaker broad He I features at late-times than is typically seen, with its late-time spectral and photometric evolution more similar to those of SNe Ic.

The modelling of the CSM light-curve component with MOSFIT, that while subject to several assumptions can inform this discussion. With the required CSM mass of $0.59^{+0.19}_{-0.14}\ \mathrm{M}_{\odot}$ easily producible through either LBV eruptive mass-loss events, which have been observed to ejecta up to a few solar masses of material (Smith 2017), though in most cases the stars seen to produce these large outbursts have high masses in tension with the low values of ejecta mass produced by the modelling (~0.08–1.30$\mathrm{M}_{\odot}$). Alternatively, if the CSM is produced largely via winds at the expected mass-loss rates of either LBV or WR stars ($\sim 1\mathrm{x}10^{-5} - 1\mathrm{x}10^{-3}\ \mathrm{M}_{\odot}\ \mathrm{yr}^{-1}$; Moriya & Maeda 2016; Smith 2017) the material could accumulate within a few thousand years, though at the relative speeds of ejection the ejecta–wind interaction would be expected to occur over several years rather than the short duration observed in LSQ13ddu. The determined progenitor radius from the modelling of $1.58^{+1.94}_{-0.80}$ au is more consistent with an extended LBV-like progenitor than WR star (Sholukhova et al. 2015), with LBV stars observed with radii 0.33–0.93 au compared to the much more compact WR stars with radii as small as a few $\mathrm{R}_{\odot}$ (~0.001 au) (Moffat & Marchenko 1996; Petrovic, Pols & Langer 2006). However, as described in Section 3.5.2, the radius value outputted by the model is highly uncertain and may have a systematic uncertainty of up to an order of magnitude depending on the input CSM configuration. Further modelling therefore is necessary to conclusively constrain the progenitor based on its estimated radius.

For the initial rapid rise and peak of LSQ13ddu to be powered largely through CSM interaction, the CSM must have been located very close to the progenitor star at the time of explosion. The CSM signatures also disappeared quickly on the time-scale of less than two weeks after maximum. This fast appearance and disappearance could suggest a very recent pre-explosion outburst (or unusually rapid mass-loss period) so that the CSM material that we see as early interaction is constrained to quite a small radius around the star. For SN 2006jc, the eruptive pre-explosion event was suggested to be caused by the coincidental eruption of an LBV companion star very shortly before the terminal explosion of the WR star. For LSQ13ddu, a binary companion in an earlier stage of evolution where mass-loss is still removing He-rich material could provide CSM of required mass and composition to generate the detected interaction signatures, through a combination of winds and/or eruptions. Though the low He I velocities observed for LSQ13ddu that are coincident with LBV wind velocities or eruption velocities are at odds with the non-detection of H emission in its spectra, a small amount at the ∼10 percent level cannot be excluded.

Some rapidly evolving transients such as iPTF16asu (Whitesides et al. 2017) have been investigated to see if their light curve could be powered by magnetar formation but it was found that the derived ejecta masses were too low (e.g. Arcavi et al. 2016). We found a similar result for LSQ13ddu, where the very low ejecta mass from the magnetar model implies an unreasonable amount of envelope stripping to produce such a low ejecta mass.

5 CONCLUSIONS

LSQ13ddu is likely a hybrid event that transitions from showing weak, narrow P-Cygni He I features on a blue continuum to showing spectra and light curves more consistent with Ic SNe with some residual He remaining in its ejecta. The rapid 4.8 d rise from explosion to a bright absolute magnitude of −19.71 ± 0.02 mag, along with the detection of narrow P-Cygni profiled He features, are properties common to SNe Ibn. Analysis of its light curve suggests that the photometric behaviour of LSQ13ddu is well described by a combination of sources: CSM interaction to power the early light curve peak and enable the rapid rise in luminosity and a component powered by the radioactive ^{56}Ni decay to explain the late-time evolution. The presence of the weak, narrow He I CSM signatures also disappeared after a few weeks, consistent with the photometric analysis showing the underlying radioactive ^{56}Ni component becoming more dominant over time. The weakness of the narrow He I features even at early times suggests the presence of less He in the surrounding environment than seen in SNe Ibn. The similarity of the later time spectra of LSQ13ddu to more normal SE-SNe indicates that the underlying SN is likely to have been produced by a heavily stripped star with the source of the CSM arising from an unseen binary companion or from a recent phase of increased mass-loss.

The population of hybrid He-interacting events has been shown to span from events with residual H within the CSM, to more stripped events lacking H but with significant He within their progenitors at the time of explosion (SN 2010al, ASASSN-15ed) to even more stripped events such as iPTF16asu (Whitesides et al. 2017). iPTF16asu displayed an early blue continuum similar to those of SNe Ibn but without He I or He II lines and then evolved to be most similar to a Ic-BL SN. LSQ13ddu falls on this continuum, with early-time spectra and photometric behaviour similar to those of a Ibn SN with weak He I lines before evolving to more closely match the behaviour of a Ic SN with some residual He within its ejecta at later times.

As ongoing high-cadence surveys continue to discover more fast evolving and transitional events interacting with He-dominated CSM, it will be essential that new theoretical models of massive stars, their mass-loss, and the probability of explosion during as LBV or WR stars are explored that can hopefully explain the diversity of these classes of events and unveil their most likely progenitor scenarios.

ACKNOWLEDGEMENTS

PC acknowledges funding from the Department for Education. KM acknowledges support from the UK Science and Technology Facility Council through an Ernest Rutherford Fellowship (ST/M005348/1) and from EU/H2020/ERC grant no. 758638. GH and DAH are supported by National Science Foundation grant AST-1313484. EYH, MS, and CA acknowledge support from the National Science Foundation under grant no. AST-1613472. T-WC acknowledges funding from the Alexander von Humboldt Foundation. MF is supported by a Royal Society – Science Foundation Ireland University Research Fellowship. GP acknowledges support by the Ministry of Economy, Development, and Tourism's Millennium Science Initiative through grant IC120009, awarded to The Millennium Institute of Astrophysics, MAS. MS is supported in part by a grant (13261) from VILLUM FONDEN and a project grant from the Independent Research Fund Denmark. MS acknowledges support from EU/FP7-ERC grant no. 615929. Based on observations collected at the European Organisation for Astronomical Research in the Southern Hemisphere, Chile as part of PESSTO, (the Public ESO Spectroscopic Survey for Transient Objects Survey) ESO program ID 188.D-3003. The CSP-II has been funded by the USA's National Science Foundation under grants AST-0306969, AST-0607438, AST-1008343, AST-1613426, AST-1613455, and AST-1613472, and in part by a Sapere Aude Level 2 grant funded by the Danish Agency for Science and Technology and Innovation (PI Stritzinger). This work makes use of the NASA/IPAC Extragalactic Database (NED), which is operated by the Jet Propulsion Laboratory, California Institute of Technology, under contract with the National Aeronautics and Space Administration. This work makes use of observations from the LCOGT Network. The work made use of Swift/UVOT data reduced by P. J. Brown and released in the Swift Optical/Ultraviolet Supernova Archive (SOUSA). SOUSA is supported by NASA's Astrophysics Data Analysis Program through grant NNX13AF35G. The Liverpool Telescope is operated on the island of La Palma by Liverpool John Moores University in the Spanish Observatorio del Roque de los Muchachos of the Instituto de Astrofisica de Canarias with financial support from the UK STFC (Project ID: PL13B10, PL13B16).

REFERENCES

Alard C., Lupton R. H., 1997, ApJ, 503, 325
Andrews J. E., Smith N., 2018, MNRAS, 477, 74
Arcavi I. et al., 2016, ApJ, 819, 35
Asplund M., Grevesse N., Sauval A. J., Scott P., 2009, ARA&A, 47, 481
Baldwin J. A., Phillips M. M., Terlevich R., 1981, PASP, 93, 5
Baltay C. et al., 2013, PASP, 125, 683
Becker A., 2015, Astrophysics Source Code Library, record ascl:1504.004
Bellm E. C. et al., 2019, PASP, 131, 018002
Bhat P. N. et al., 2016, ApJS, 223, 28
Boyle A., Sim S. A., Hachinger S., Kerzendorf W., 2017, A&A, 599, 1
Brown T. M. et al., 2013, PASP, 125, 1031
Brown P. J., Breeveld A. A., Holland S., Kuin P., Pritchard T., 2014, Astrophys. Space Sci., 354, 89
Buzzoni B. et al., 1984, ESO Messenger, 38, 9
Cano Z., Wang S.-Q., Dai Z.-G., Wu X.-F., 2017, Adv. Astron., 2017, 1
Chatzopoulos M., 2018, TigerFit, https://github.com/manolis07gr/TigerFit
Chatzopoulos E., Wheeler J. C., Vinko J., Horvath Z. L., Nagy A., 2013, AJ, 773, 76
Chevalier R. A., Irwin C. M., 2011, ApJ, 729, L6
Childress M. J. et al., 2016, Publ. Astron. Soc. Aust., 33, 055
Chugai N. N., 2009, MNRAS, 400, 866

Crowther P. A., 2007, ARA&A, 45, 177

De K. et al., 2018, Science, 362, 201

Dopita M., Hart J., McGregor P., Oates P., Bloxham G., Jones D., 2007, Astrophys. Space Sci., 310, 255

Dressler A. et al., 2011, PASP, 123, 288

Drout M. R. et al., 2014, ApJ, 794, 23

Fermi GRB Team, 2013, GCN/Fermi Notice: GRB 131123A, https://gcn.gsfc.nasa.gov/other/406904521.fermi

Fisher A. K., 2000, PhD thesis, Univ. Oklahoma

Fitzpatrick E. L., 1999, PASP, 111, 63

Foley R. J., Smith N., Ganeshalingam M., Li W., Chornock R., Filippenko A. V., 2007, ApJ, 657, L105

Foreman-Mackey D., Hogg D. W., Lang D., Goodman J., 2013, PASP, 125, 306

Freudling W., Romaniello M., Bramich D. M., Ballester P., Forchi V., García-Dabló C. E., Moehler S., Neeser M. J., 2013, A&A, 559, A96

Ginzburg S., Balberg S., 2012, ApJ, 757, 178

Gruber D. et al., 2014, ApJS, 211

Guillochon J., Nicholl M., Villar V. A., Mockler B., Narayan G., Mandel K. S., Berger E., Williams P. K. G., 2018, ApJS, 236, 6

Hamuy M. et al., 2006, PASP, 118, 2

Henden A. A., Welch D. L., Terrell D., Levine S. E., 2009, in AAS Meeting Abstracts #214, p. 407.02

Hosseinzadeh G. et al., 2017, ApJ, 836, 158

Hosseinzadeh G., McCully C., Zabludoff A. I., Arcavi I., French K. D., Howell D. A., Berger E., Hiramatsu D., 2019, ApJ, 871, L9

Hsiao E. Y. et al., 2019, PASP, 131, 014002

Hunter D. J. et al., 2009, A&A, 508, 371

Jenness T., Economou F., 2015, Astron. Comput., 9, 40

Jones E., Oliphant T., Peterson P., Others, 2001, SciPy: Open source scientific tools for Python, http://www.scipy.org/

Jones D. H. et al., 2009, MNRAS, 399, 683

Karamehmetoglu E. et al., 2017, A&A, 602, A93

Kasliwal M. M. et al., 2010, ApJ, 723, L98

Kauffmann G. et al., 2003, MNRAS, 346, 1055

Kausch W. et al., 2015, A&A, 576, A78

Kewley L. J., Dopita M. A., Sutherland R. S., Heisler C. A., Trevena J., 2001, ApJ, 556, 121

Lyman J. D., Bersier D., James P. A., Mazzali P. A., Eldridge J. J., Fraser M., Pian E., 2016, MNRAS, 457, 328

Makarov D., Prugniel P., Terekhova N., Courtois H., Vauglin I., 2014, A&A, 570, A13

McCully C., Volgenau N. H., Harbeck D.-R., Lister T. A., Saunders E. S., Turner M. L., Siiverd R. J., Bowman M., 2018, in Guzman J. C., Ibsen G., eds, Proc. SPIE 10707, Software and Cyberinfrustructure for Astronomy V. SPIE, Bellingham, p. 141

Meynet G., Maeder A., 2005, A&A, 429, 581

Modjaz M. et al., 2014, AJ, 147, 99

Modjaz M., Liu Y. Q., Bianco F. B., Graur O., 2016, ApJ, 832, 108

Moffat A. F. J., Marchenko S. V., 1996, A&A, 522, 433

Moorwood A., Cuby J., Lidman C., 1998, ESO Messenger, 53, 1

Moriya T. J., Maeda K., 2016, ApJ, 824, 100

Moriya T. J. et al., 2017, MNRAS, 466, 2085

Nadyozhin D. K., 1994, ApJS, 92, 527

Nicholl M., 2018, Res. Notes Am. Astron. Soc., 2, 230

Nicholl M., Guillochon J., Berger E., 2017, ApJ, 850, 55

Oemler A., Clardy K., Kelson D., Walth G., Villanueva E., 2017, Astrophysics Source Code Library, record ascl:1705.001

Paciesas W. S. et al., 1999, ApJS, 122, 465

Paciesas W. S. et al., 2012, ApJS, 199

Pastorello A. et al., 2007, Nature, 447, 829

Pastorello A. et al., 2008a, MNRAS, 389, 113

Pastorello A. et al., 2008b, MNRAS, 389, 131

Pastorello A. et al., 2015a, MNRAS, 449, 1921

Pastorello A. et al., 2015b, MNRAS, 449, 1941

Pastorello A. et al., 2015c, MNRAS, 449, 1954

Pastorello A. et al., 2015d, MNRAS, 453, 3650

Pastorello A. et al., 2016, MNRAS, 456, 853

Perez F., Bagish A., Bredthauer G., Espoz J., Jones P., Pinto P., 2012, in Larry M. S., Roberto G., Helen J. H., eds, Proc. SPIE Conf. Ser., Vol. 8444, Ground-based and Airborne Telescopes IV. SPIE, Bellingham, p. 84444H

Petrovic J., Pols O., Langer N., 2006, A&A, 450, 219

Pettini M., Pagel B. E. J., 2004, MNRAS, 348, L59

Phillips M. M. et al., 2019, PASP, 131, 014001

Poznanski D. et al., 2009, Science, 327, 58

Prentice S. J. et al., 2016, MNRAS, 458, 2973

Prentice S. J. et al., 2018a, MNRAS, 478, 4162

Prentice S. J. et al., 2018b, ApJ, 865, L3

Prentice S. J. et al., 2019, MNRAS, 485, 1559

Pursiainen M. et al., 2018, MNRAS, 481, 894

Rest A. et al., 2018, Nat. Astron., 2, 307

Rochowicz K., Niedzielski A., 1999, Acta Astron., 45, 307

Sahu D. K., Tanaka M., Anupama G. C., Gurugubelli U. K., Nomoto K., 2009, ApJ, 697, 676

Sanders N. E. et al., 2013, ApJ, 769, 39

Scalzo R. A. et al., 2014, MNRAS, 445, 30

Schlafly E. F., Finkbeiner D. P., 2011, ApJ, 737

Schlegel E. M., 1990, MNRAS, 244, 269

Shappee B. J. et al., 2014, ApJ, 788, 48

Sholukhova O., Bizyaev D., Fabrika S., Sarkisyan A., Malanushenko V., Valeev A., 2015, MNRAS, 447, 2459

Simcoe R. A. et al., 2013, PASP, 125, 270

Smartt S. J. et al., 2014, A&A, 579, A40

Smette A. et al., 2015, A&A, 576, A77

Smith N., 2014, ARA&A, 52, 487

Smith N., 2017, Interacting Supernovae: Types IIn and Ibn. Springer International Publishing, Cham, p. 403

Smith N., Mauerhan J. C., Silverman J. M., Ganeshalingam M., Filippenko A. V., Cenko S. B., Clubb K. I., Kandrashoff M. T., 2012, MNRAS, 426, 1905

Steele I. A. et al., 2004, in Oschmann J. M. Jr, ed., Proc. SPIE Conf. Ser., Vol. 5489, Ground-based Telescopes. SPIE, Bellingham, p. 679

Swartz D. A., Sutherland P. G., Harkness R. P., 1995, ApJ, 446, 766

Taddia F. et al., 2015, A&A, 580, A131

Tauris T. M., Langer N., Podsiadlowski P., 2015, MNRAS, 451, 2123

Thomas R. C., Nugent P. E., Meza J. C., 2011, PASP, 123, 237

Tonry J. L. et al., 2012, ApJ, 750, 99

Tonry J. L. et al., 2018, PASP, 130, 064505

Umeda H., Nomoto K., 2008, ApJ, 673, 1014

Valenti S. et al., 2016, MNRAS, 459, 3939

van Loon J. T., 2006, in Lamers H. J. G. L. M., Langer N., Nugis T., Annuk K., eds, Stellar Evolution at Low Metallicity: Mass Loss, Explosions, Cosmology ASP Conference Series, Vol. 353, Proc. of the Conference Held 15-19 August, 2005 in Tartu, Estonia. ASP Conference Series, San Francisco, p. 211

Vernet J. et al., 2011, A&A, 536, A105

Villar V. A., Berger E., Metzger B. D., Guillochon J., 2017, ApJ, 849, 70

Wang L. J. et al., 2017, ApJ, 851, 54

Wheeler J. C., Johnson V., Clocchiatti A., 2015, MNRAS, 450, 1295

Whitesides L. et al., 2017, ApJ, 851, 107

Woosley S., Bloom J., 2006, ARA&A, 44, 507

Woosley S. E., Eastman R. G., Weaver T. A., Pinto P. A., 1994, ApJ, 429, 300

Woosley S. E., Eastman R. G., Schmidt B. P., 1999, ApJ, 516, 788

Yaron O., Gal-Yam A., 2012, PASP, 124, 668

[1] *Astrophysics Research Centre, School of Mathematics and Physics, Queen's University Belfast, Belfast BT7 1NN, UK*

[2] *School of Physics, Trinity College Dublin, Dublin 2, Ireland*

[3] *School of Physics and Astronomy, Cardiff University, The Parade, Cardiff CF24 3AA, UK*

[4] *Carnegie Observatories, Las Campanas Observatory, Casilla 601, La Serena, Chile*

[5] *Center for Astrophysics | Harvard & Smithsonian, 60 Garden Street, Cambridge, MA 02138-1516, USA*

[6]*Department of Physics, Florida State University, Tallahassee, FL 32306, USA*
[7]*Tuorla Observatory, Department of Physics and Astronomy, University of Turku, FI-20014 Turku, Finland*
[8]*Division of Physics, Mathematics and Astronomy, California Institute of Technology, Pasadena, CA 91125, USA*
[9]*Lawrence Berkeley National Laboratory, Berkeley, CA 94720, USA*
[10]*Department of Physics, Yale University, 217 Prospect Street, New Haven, CT 06250-8121, USA*
[11]*School of Physics and Astronomy, Tel Aviv University, Tel Aviv 69978, Israel*
[12]*Observatories of the Carnegie Institution for Science, 813 Santa Barbara St, Pasadena, CA 91101, USA*
[13]*School of Physics, O'Brien Centre for Science North, University College Dublin, Belfield, Dublin 4, Ireland*
[14]*Max-Planck-Institut für Extraterrestrische Physik, Giessenbachstraße 1, D-85748 Garching, Germany*
[15]*Laboratory of Observational Cosmology, Code 665, NASA Goddard Space Flight Center, Greenbelt, MD 20771, USA*
[16]*Las Cumbres Observatory, 6740 Cortona Drive, Suite 102, Goleta, CA 93117-5575, USA*
[17]*Department of Physics, University of California, Santa Barbara, CA 93106-9530, USA*
[18]*Department of Physics and Astronomy, Aarhus University, Ny Munkegade 120, DK-8000 Aarhus C, Denmark*
[19]*The Oskar Klein Centre & Department of Astronomy, Stockholm University, AlbaNova, SE-106 91 Stockholm, Sweden*
[20]*Department of Physics, University of Warwick, Coventry CV4 7AL, UK*
[21]*Departamento de Ciencias Físicas, Universidad Andres Bello, Avda. Fernández Concha 700, 7591538 Santiago, Chile*
[22]*Millennium Institute of Astrophysics, Nuncio Monsenor Sótero Sanz 100, Providencia, 8320000 Santiago, Chile*
[23]*School of Physics and Astronomy, University of Southampton, Southampton SO17 1BJ, UK*

This paper has been typeset from a TEX/LATEX file prepared by the author.